

# Late Neogene exhumation and relief development of the Aar and Aiguilles Rouges massifs (Swiss Alps) from low-temperature thermochronology modeling and $^4\text{He}/^3\text{He}$ thermochronometry

Pierre G. Valla,<sup>1,2</sup> Peter A. van der Beek,<sup>1</sup> David L. Shuster,<sup>3,4</sup> Jean Braun,<sup>1</sup> Frédéric Herman,<sup>2</sup> Laurent Tassan-Got,<sup>5</sup> and Cécile Gautheron<sup>6</sup>

Received 28 March 2011; revised 1 November 2011; accepted 6 November 2011; published 12 January 2012.

[1] The late Neogene–Quaternary exhumation history of the European Alps is the subject of controversial findings and interpretations, with several thermochronological studies arguing for long-term steady state exhumation rates, while others have pointed to late Miocene–Pliocene exhumation pulses associated with tectonic and/or climatic changes. Here, we perform inverse thermal-kinematic modeling on dense thermochronological data sets combining apatite fission track (AFT) data from the literature and recently published apatite (U–Th–Sm)/He (AHe) data along the upper Rhône valley (Aar and Aiguilles Rouges massifs, Swiss Alps) in order to derive precise estimates on the denudation and relief history of this region. We then apply forward numerical modeling to interpret cooling paths quantified from apatite  $^4\text{He}/^3\text{He}$  thermochronometry, in terms of denudation and relief-development scenarios. Our modeling results highlight the respective benefits of using AFT/AHe thermochronology data and  $^4\text{He}/^3\text{He}$  thermochronometry for extracting quantitative denudation and relief information. Modeling results suggest a late Miocene exhumation pulse lasting until  $\sim 8$ – $10$  Ma, consistent with recently proposed exhumation histories for other parts of the European Alps, followed by moderate ( $\sim 0.3$ – $0.5$  km Myr<sup>−1</sup>) denudation rates during the late Miocene/Pliocene. Both inverse modeling and  $^4\text{He}/^3\text{He}$  data reveal that the late stage exhumation of the studied massifs can be explained by a significant increase ( $\sim 85$ – $100\%$ ) in local topographic relief through efficient glacial valley carving. Modeling results quantitatively constrain Rhône valley carving to 1–1.5 km since  $\sim 1$  Ma. We postulate that recent relief development within this part of the Swiss Alps is climatically driven by the onset of major Alpine glaciations at the mid-Pleistocene climate transition.

**Citation:** Valla, P. G., P. A. van der Beek, D. L. Shuster, J. Braun, F. Herman, L. Tassan-Got, and C. Gautheron (2012), Late Neogene exhumation and relief development of the Aar and Aiguilles Rouges massifs (Swiss Alps) from low-temperature thermochronology modeling and  $^4\text{He}/^3\text{He}$  thermochronometry, *J. Geophys. Res.*, 117, F01004, doi:10.1029/2011JF002043.

## 1. Introduction

[2] Understanding the long-term evolution of active mountain belts requires precise identification and quantification of the potential couplings between tectonics, climate and erosion [e.g., *Beaumont et al.*, 1992; *Willett*, 1999; *Whipple and Meade*, 2006; *Whipple*, 2009]. One key

illustration of this problem is the ongoing debate on the potential links between the late Cenozoic increase in global sediment budgets [e.g., *Hay et al.*, 1988; *Zhang et al.*, 2001; *Molnar*, 2004], and Pliocene–Pleistocene climate or tectonic changes enhancing mountain belt denudation [*Molnar and England*, 1990; *Raymo and Ruddiman*, 1992; *Zhang et al.*, 2001].

[3] A similar increase in foreland sedimentation rates has been reported for the European Alps since  $\sim 5$  Ma [*Kuhlemann et al.*, 2002; *Willett et al.*, 2006], in concordance with the initiation of exhumation in the northern Alpine foreland basin [*Cederbom et al.*, 2004, 2011], cessation of folding in the Jura Mountains [*Becker*, 2000] and possibly reactivation of deformation in the internal part of the orogen [*Willett et al.*, 2006]. A compilation of in situ apatite fission track (AFT) thermochronology data from the western and central Alps, and an analysis of regional age-elevation trends within the data [*Vernon et al.*, 2008] also indicated a Pliocene exhumation pulse in the external part of the range. However,

<sup>1</sup>Institut des Sciences de la Terre, Université Joseph Fourier, Grenoble, France.

<sup>2</sup>Geologisches Institut, ETH Zurich, Zurich, Switzerland.

<sup>3</sup>Berkeley Geochronology Center, Berkeley, California, USA.

<sup>4</sup>Department of Earth and Planetary Science, University of California, Berkeley, California, USA.

<sup>5</sup>Institut de Physique Nucléaire, Université Paris Sud, CNRS/IN2P3, Orsay, France.

<sup>6</sup>Interactions et Dynamique des Environnements de Surface, Université Paris Sud, CNRS, Orsay, France.

the timing of both sedimentation and exhumation pulses appears to be spatially diachronous for the Western and central Alps; sedimentation rate increases occurred at around 5 and 1 Ma [Kuhlemann et al., 2002], while accelerations in denudation rates started between 6.5 and 2.5 Ma for different regions [Vernon et al., 2008]. Similarly, local studies using in situ low-temperature thermochronology data have led to contrasting conclusions regarding Neogene exhumation histories, with inconsistent timing and rates of exhumation pulses, or no such pulses at all, reported in different parts of the Western and central Alps [e.g., Wagner et al., 1977; Hurford, 1986, 1991; Bigot-Cormier et al., 2006; Glotzbach et al., 2008, 2010, 2011a; Reinecker et al., 2008; Vernon et al., 2009; van der Beek et al., 2010]. Moreover, detrital thermochronology results suggest constant orogen-scale exhumation rates in the Western European Alps since 10–15 Ma [Bernet et al., 2001, 2009; Glotzbach et al., 2011b].

[4] It thus appears necessary to provide tighter quantitative constraints on the late Neogene exhumation of the Alpine massifs in order to (1) better understand the apparent spatial heterogeneity in exhumation histories [e.g., Vernon et al., 2008] and (2) identify the potential climatic and/or tectonic forcing for the acceleration in exhumation within the Western and central Alps. The nature of exhumation triggers for the late Neogene evolution of the Alps has been widely discussed in the literature, with contrasting interpretations. Persaud and Pfiffner [2004], and more recently Schlunegger and Mosar [2011], have linked a late Miocene–Pliocene acceleration in denudation rates to ongoing deformation and crustal accretion within the Swiss central Alps, while Reinecker et al. [2008] attributed mid-Pliocene tectonic denudation in the same area to orogen-perpendicular extension along major faults (e.g., the Rhône-Simplon fault [Mancktelow, 1985, 1992]). On the other hand, the Pliocene increase in both exhumation and sedimentation rates has been interpreted as a response to a major climatic change, associated with gradual climate cooling in the Pliocene [e.g., Zhang et al., 2001; Haug et al., 2005] and a transition toward wetter conditions [Driscoll and Haug, 1998] that could have enhanced mountain belt denudation [e.g., Molnar and England, 1990]. Moreover, recent studies have suggested that significant valley carving following the onset of Pleistocene glaciations may have contributed to the late stage exhumation of the Alpine massifs [e.g., Haeuselmann et al., 2007; Glotzbach et al., 2011a; Valla et al., 2011a]. In particular, Valla et al. [2011a] have recently used apatite  $^4\text{He}/^3\text{He}$  thermochronometry [Shuster and Farley, 2005] to show that the Rhône Valley in the Swiss central Alps was deepened by 1–1.5 km since  $\sim 1$  Ma, while higher parts of the landscape remained preserved.

[5] Here, we perform forward and inverse numerical modeling using published low-temperature thermochronology data (apatite fission track (AFT) and apatite (U-Th-Sm)/He data (AHe)), combined with apatite  $^4\text{He}/^3\text{He}$  thermochronometry, to (1) constrain the late Neogene exhumation history of the central Alps (Aiguilles Rouges and Aar massifs) and (2) assess the impact of Pliocene climate change and/or Pleistocene glaciations on the late stage exhumation and topographic evolution of these massifs. We use a recently developed method coupling the thermal-kinematic model Pecube [Braun, 2003] with an iterative inverse approach [Sambridge, 1999a, 1999b] to quantitatively extract information on both

exhumation and relief histories from the thermochronology data [e.g., Herman et al., 2007, 2010a; Valla et al., 2010a; van der Beek et al., 2010; Glotzbach et al., 2011a], implementing the control of alpha recoil damage on He diffusion kinetics in apatite [Shuster et al., 2006; Flowers et al., 2009; Gautheron et al., 2009]. We first compile AFT data from the literature [Wagner et al., 1977; Rahn, 1994; Reinecker et al., 2008] with AHe data we reported in a recent study [Valla et al., 2011a] and use these as input for the numerical inversions. We then interpret cooling histories quantified from apatite  $^4\text{He}/^3\text{He}$  data [Valla et al., 2011a] in terms of late Neogene exhumation and quantitatively constrain the Pleistocene relief increase observed by Valla et al. [2011a] using forward thermal-kinematic modeling. We finally discuss the results from the two approaches to assess how to provide optimal constraints on both the regional late Neogene exhumation history and local relief development during Pliocene–Pleistocene times.

[6] In the following, we first present the study area and discuss the selected thermochronology data and their qualitative interpretation in terms of apparent exhumation rates. We then summarize our two modeling approaches and show the predictions derived from the thermochronology data for the late Neogene exhumation histories of the Aiguilles Rouges and Aar massifs. Finally, we attempt to precisely quantify both the timing and amplitude of the topographic change associated with late Pliocene–Pleistocene glaciations.

## 2. Geological and Geomorphic Setting

[7] The Aar and Aiguilles Rouges massifs (Figure 1a) are two of the Alpine “external crystalline massifs” (ECMs): blocks of European crystalline basement that are exposed in an orogen-parallel string of massifs on the northern and western rim of the Alps [e.g., Schmid et al., 2004]. The Aar and Aiguilles Rouges massifs comprise pre-Variscan and Variscan crystalline rocks and Paleozoic to Tertiary sedimentary series [e.g., von Raumer and Neubauer, 1993] that have been buried and metamorphosed by overthrusting of the Helvetic and Penninic nappes during the Alpine collision [Abrecht, 1994; Frey and Ferreira Maehlmann, 1999]. Ongoing collision resulted in Oligocene–Miocene exhumation of the ECMs from  $\sim 8$ –15 km depth [e.g., Schmid and Kissling, 2000; Leloup et al., 2005] along major crustal-scale faults.

[8] The Neogene tectonic evolution of the study area is related to the activity of the Rhône-Simplon fault (Figure 1a), a southward-dipping low-angle detachment fault [e.g., Mancktelow, 1985, 1992; Seward and Mancktelow, 1994] accommodating tectonic denudation since the early Miocene until Pliocene to recent times [Reinecker et al., 2008; Campani et al., 2010]. However, the late Neogene activity of this structure is controversial, with some studies arguing for a Pliocene acceleration of tectonic denudation [Soom, 1990; Reinecker et al., 2008], while others suggest a decrease in Rhône-Simplon fault activity during the late Neogene [e.g., Mancktelow, 1992; Campani et al., 2010]. The present-day kinematics of the area reveals no active compression [Calais et al., 2002; Nocquet and Calais, 2004] and orogen-perpendicular extension [e.g., Champagnac et al., 2004; Sue et al., 2007]. Geodetic measurements do record significant present-day rock

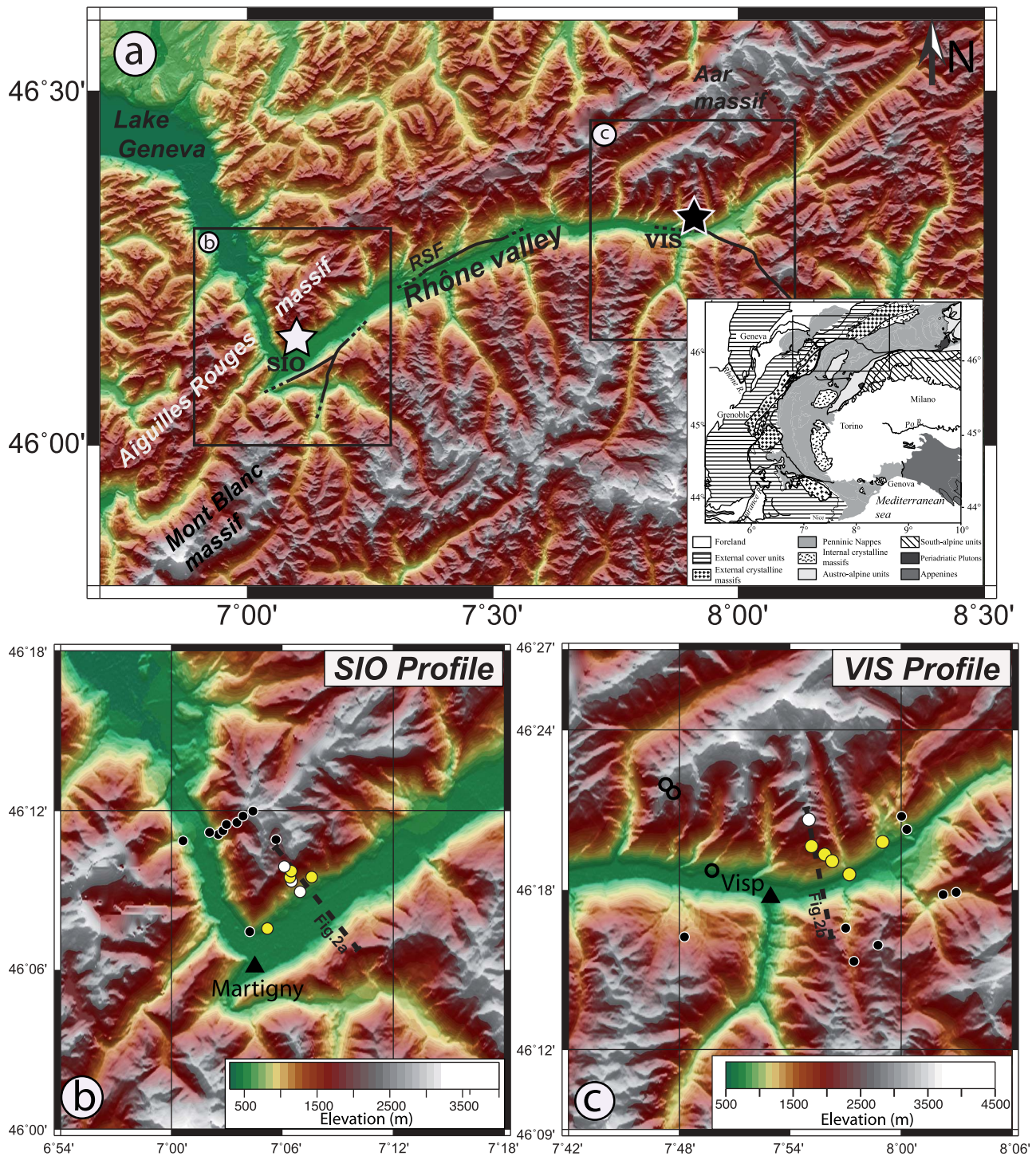


**Figure 1.** Topography and sample locations. (a) Relief map of the studied area in the Swiss Alps. Stars represent SIO (white) and VIS (black) sampling sites along the Rhône valley. The black boxes outline the model domains shown in Figures 1b and 1c. Black lines indicate the location of the Rhône-Simplon fault (RSF) along the Rhône valley [Mancktelow, 1985, 1992; Seward and Mancktelow, 1994]. Inset shows location of the study area within the European Alps and major litho-tectonic units [Schmid et al., 2004]. (b) Sample locations for SIO and (c) VIS areas; yellow circles: AHe and  $^4\text{He}/^3\text{He}$  data; white circles: AHe data only; black circles: AFT data from the literature (black circles in Figure 1b from Rahn [1994]; open circles in Figure 1c from Reinecker et al. [2008] and black circles from Wagner et al. [1977], see Figure 2 and Tables 1 and 2 for details). Cross profiles shown in Figure 2 are also indicated (dashed lines in Figures 1b and 1c).

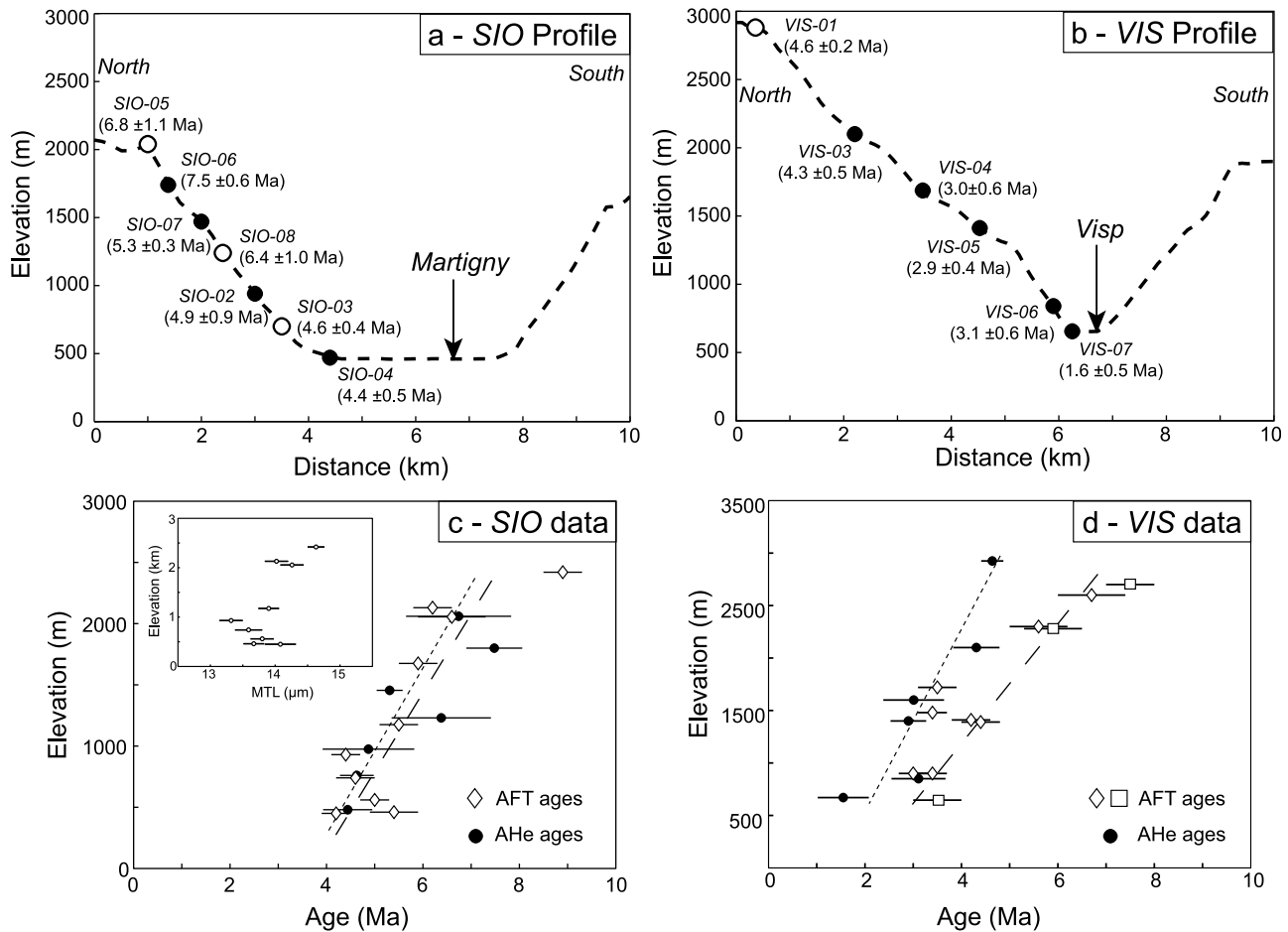


**Figure 2.** Topographic cross-profiles of the Rhône valley at the (a) SIO and (b) VIS sampling sites showing apatite samples from *Valla et al.* [2011a] (black: AHe +  $^4\text{He}/^3\text{He}$  data; open: AHe data only; AHe ages in brackets). Thermochronological data for the VIS and SIO areas. (c) SIO age-elevation profiles for AHe (black circles) and AFT [*Rahn*, 1994] data (open diamonds). Inset shows mean fission track lengths of AFT samples [*Rahn*, 1994]. (d) VIS age-elevation profiles for AHe (black circles) and AFT data (open squares are from *Reinecker et al.* [2008]; open diamonds are from *Wagner et al.* [1977]). Regression lines show weighted linear fits to the data (dotted line: AHe ages; dashed line: AFT ages). See Tables 1 and 2 for sample details.

uplift rates of  $>1 \text{ mm yr}^{-1}$  across most of the Swiss Alps [*Kahle et al.*, 1997; *Schlatter et al.*, 2005].

[9] Published thermochronology data include zircon fission track (ZFT) ages of  $>100 \text{ Ma}$  in the Aiguilles Rouges massif [*Rahn*, 1994] and ranging from 10 to  $\sim 100 \text{ Ma}$  in the Aar massif [*Michalski and Soom*, 1990; *Glottzbach et al.*, 2010]. The ZFT thermochronometric system has thus been only partially reset during Alpine collision, which constrains the Cenozoic exhumation of the area to a maximum of  $\sim 9\text{--}10 \text{ km}$  (adopting a ZFT closure temperature of  $\sim 210\text{--}240^\circ\text{C}$  [*Brandon et al.*, 1998; *Bernet*, 2009]) and a geothermal gradient of  $\sim 25^\circ\text{C km}^{-1}$ ). AFT and AHe ages range from  $\sim 2$  to  $10 \text{ Ma}$  in the Aar massif [*Wagner et al.*, 1977; *Michalski and Soom*, 1990; *Soom*, 1990; *Reinecker et al.*, 2008; *Vernon et al.*, 2009; *Glottzbach et al.*, 2010], similar to AFT ages for the Aiguilles Rouges massif [*Soom*, 1990; *Rahn*, 1994; *Seward and Mancktelow*, 1994]. Age-elevation relationships [*Wagner et al.*, 1977; *Hurford*, 1986, 1991; *Reinecker et al.*, 2008] and numerical thermal modeling [*Vernon et al.*, 2009; *Glottzbach et al.*, 2010] both suggest fairly constant

exhumation rates of  $\sim 0.3\text{--}0.7 \text{ km Myr}^{-1}$  through the late Neogene, with a potential acceleration during the late Pliocene [*Reinecker et al.*, 2008; *Glottzbach et al.*, 2010; *Pignalosa et al.*, 2011]. However, none of these studies, except for that of *Vernon et al.* [2009], considered the effects of potential topographic relief change on Neogene exhumation, and the relief history has not been studied in detail for these two massifs.

[10] The topography of the Swiss Alps presents high relief with peaks reaching up to  $4000 \text{ m}$  and valley bottoms lying at  $\sim 400\text{--}700 \text{ m}$  elevation (Figure 1a). Both the drainage pattern and the first-order relief organization are strongly controlled by lithological and tectonic structure [*Kühni and Pfiffner*, 2001a, 2001b]; however, the present-day landscape reveals a strong imprint of late Pleistocene glaciations with typical U-shaped valleys (Figures 2a and 2b) and major overdeepenings within the upper Rhône catchment [*Finckh and Frei*, 1991; *Pfiffner et al.*, 1997; *Rosselli and Olivier*, 2003] that are thought to have been carved by thick, large and erosive glaciers [e.g., *Kelly et al.*, 2004]. The amount of

**Table 1.** Apatite Fission Track and (U-Th-Sm)/He (AHe) Data for the VIS Area<sup>a</sup>

Sample	Longitude (°E)	Latitude (°N)	Elevation (m)	Tectonic Unit	AFT Age $\pm 1\sigma$ (Ma)	AHe Age $\pm 1\sigma$ (Ma)	eU/a/UTh (ppm/ $\mu\text{m}$ )	Source
VIS-01	7.91668	46.3439	2925	Aar massif	/	4.6 $\pm$ 0.2	50/58.0/1.9	[1]
VIS-03	7.9191	46.32732	2100	Aar massif	/	4.3 $\pm$ 0.5	62/74.2/2.9	[1]
VIS-04	7.93106	46.32198	1700	Aar massif	/	3.0 $\pm$ 0.6	29/70.4/0.9	[1]
VIS-05	7.93781	46.31788	1400	Aar massif	/	2.9 $\pm$ 0.4	25/68.5/0.8	[1]
VIS-06	7.98339	46.33	850	Aar massif	/	3.1 $\pm$ 0.6	85/101.3/1.3	[1]
VIS-07	7.95333	46.30967	670	Aar massif	/	1.6 $\pm$ 0.5	38/71.3/0.6	[1]
KAW-0400	7.95168	46.27076	1480	Monte Leone nappe	3.4 $\pm$ 0.3	/	/	[2]
KAW-0401	7.80704	46.27132	2300	Monte Leone nappe	5.6 $\pm$ 0.6	/	/	[2]
KAW-0399	7.95348	46.25546	1720	Monte Leone nappe	3.5 $\pm$ 0.4	/	/	[2]
KAW-0409	7.98467	46.26251	2600	Monte Leone nappe	6.7 $\pm$ 0.7	/	/	[2]
KAW-0164	8.0494	46.29771	1410	Berisal series	4.2 $\pm$ 0.4	/	/	[2]
KAW-0165	8.04265	46.29766	1390	Berisal series	4.4 $\pm$ 0.4	/	/	[2]
KAW-0315	8.00583	46.33651	900	Aar massif	3.0 $\pm$ 0.3	/	/	[2]
KAW-0360	8.00365	46.34158	900	Aar massif	3.4 $\pm$ 0.3	/	/	[2]
LBS-17	7.78339	46.34588	2700	Aar massif	7.5 $\pm$ 0.5	/	/	[3]
LBS-18	7.78909	46.34325	2280	Aar massif	5.9 $\pm$ 0.6	/	/	[3]
LB-12	7.82646	46.31151	645	Aar massif	3.5 $\pm$ 0.5	/	/	[3]

<sup>a</sup>Sources are 1: *Valla et al.* [2011a]; 2: *Wagner et al.* [1977]; 3: *Reinecker et al.* [2008]. Effective uranium concentration (eU), equivalent sphere radius (a), and U/Th ratio (UTh) are used for AHe age predictions using a radiation-damage model [*Gautheron et al.*, 2009].

relief development during Pleistocene glaciations has mostly been evaluated from the massif-scale geophysical relief [e.g., *Small and Anderson*, 1998; *Brocklehurst and Whipple*, 2002]. Recent studies have proposed 1–1.5 km of Quaternary relief increase in the Western and central Alps [*Champagnac et al.*, 2007; *van der Beek and Bourbon*, 2008], in agreement with quantitative constraints on local Pleistocene valley carving [*Hauselmann et al.*, 2007; *Valla et al.*, 2011a].

[11] The present-day landscape also shows evidence for efficient postglacial relief rejuvenation [*Schlunegger and Hinderer*, 2003; *Norton et al.*, 2010] by hillslope and fluvial processes [e.g., *Korup and Schlunegger*, 2007; *Delunel et al.*, 2010; *Valla et al.*, 2010b]. Moreover, late Pleistocene to Holocene sediment fluxes [*Hinderer*, 2001; *Schlunegger and Hinderer*, 2001] and catchment-integrated denudation rates from cosmogenic <sup>10</sup>Be [*Wittmann et al.*, 2007] closely match geodetic rock-uplift rates [*Schlatter et al.*, 2005], suggesting a potential coupling between erosion and uplift for late Pleistocene to recent times. Several studies have proposed that modern rock uplift measured within the Western and central Alps at least partly results from the isostatic response to surface unloading by Pleistocene [*Champagnac et al.*, 2007, 2008] or Holocene [*Champagnac et al.*, 2009; *Norton et al.*, 2010] erosion, as well as late glacial to Holocene glacier retreat [*Gudmundsson*, 1994; *Barletta et al.*, 2006].

### 3. Numerical Modeling of Thermochronology Data

#### 3.1. AHe and AFT Thermochronology

[12] The AHe and AFT systems are characterized by closure temperatures ( $T_c$ ) ranging from 60–80°C to 100–120°C, respectively [*Gallagher et al.*, 1998; *Farley*, 2002]. However, recent studies have shown that He diffusivity and consequently the AHe closure temperature are linked to the amount of radiation ( $\alpha$  recoil) damage accumulated in the apatite crystal [*Shuster et al.*, 2006; *Flowers et al.*, 2009; *Gautheron et al.*, 2009]. The amount of radiation damage itself depends on the effective U content (as it is created by  $\alpha$  decay of U and Th) and the thermal history, because radiation damage can be

thermally annealed [*Flowers et al.*, 2009; *Gautheron et al.*, 2009; *Shuster and Farley*, 2009]. As an example, different effective Uranium concentrations (eU = [U] + 0.24 [Th], in which each parent nuclide concentration is weighted by its  $\alpha$  production) of 10, 50, 100, 150 and 200 ppm, combined with a 10°C Myr<sup>-1</sup> cooling rate and an assumed 60  $\mu\text{m}$  grain radius, will lead to  $T_c$  values of  $\sim$ 74, 80, 83, 86, and 87°C, respectively [*Gautheron et al.*, 2009], varying from the  $T_c \approx 74^\circ\text{C}$  obtained for conventional diffusion parameters [*Farley*, 2000].

[13] Numerical algorithms have recently been developed to simulate the radiation damage effect on He retention [*Flowers et al.*, 2009; *Gautheron et al.*, 2009]. *Valla et al.* [2011a] used the Radiation Damage Accumulation and Annealing Model (RDAAM) algorithm [*Flowers et al.*, 2009] to interpret <sup>4</sup>He/<sup>3</sup>He and AHe data in terms of cooling paths. Here, we combine a similar numerical approach [*Gautheron and Tassan-Got*, 2010] with the Pecube model for AHe age predictions. Both models are very similar and use the effective U concentration, U/Th ratio, and the sphere-equivalent radius (eU, UTh and a, respectively (Tables 1 and 2)) as well as a thermal history as input parameters [*Flowers et al.*, 2009; *Gautheron et al.*, 2009]. The main difference between the two approaches concerns the assumed dependence between radiation damage defects and He retention within the crystal lattice. *Flowers et al.* [2009] adopted a cubic form from empirical data [*Shuster et al.*, 2006], while *Gautheron et al.* [2009] proposed a physically derived linear dependence between the creation of lattice defects and the amount of trapped He. In summary, both codes are very close in their treatment of the radiation damage effect on He retention; we thus decided (for computational reasons) to use the model of *Gautheron and Tassan-Got* [2010] in some of the following Pecube simulations.

#### 3.2. Low-Temperature Thermochronology Data Compilation

[14] In this study, we combine recently published AHe data sampled along two elevation profiles (VIS and SIO sites, see Figures 1 and 2 and *Valla et al.* [2011a]) with AFT data from the literature [*Wagner et al.*, 1977; *Rahn*, 1994; *Reinecker et al.*, 2008]. We define two specific areas for thermal-kinematic modeling (Figure 1a): (1) an area centered on the

**Table 2.** Apatite Fission Track, (U-Th-Sm)/He (AHe), and Mean Track Length Data for the SIO Area<sup>a</sup>

Sample	Longitude (°E)	Latitude (°N)	Elevation (m)	Tectonic Unit	AFT Age $\pm 1\sigma$ (Ma)	MTL $\pm 1\sigma$ ( $\mu\text{m}$ )	AHe Age $\pm 1\sigma$ (Ma)	eU/a/UTh (ppm/ $\mu\text{m}$ )	Source
SIO-05	7.10163	46.16485	2060	Aiguilles Rouges Massif	/	/	6.7 $\pm$ 1.1	84/80.3/24.1	[1]
SIO-06	7.1081	46.16192	1800	Aiguilles Rouges Massif	/	/	7.5 $\pm$ 0.6	149/79.3/21.1	[1]
SIO-07	7.1068	46.15813	1455	Aiguilles Rouges Massif	/	/	5.3 $\pm$ 0.3	151/71.6/22.0	[1]
SIO-08	7.10825	46.15562	1230	Aiguilles Rouges Massif	/	/	6.4 $\pm$ 1.0	213/63.4/17.4	[1]
SIO-02	7.12653	46.15828	975	Aiguilles Rouges Massif	/	/	4.9 $\pm$ 1.0	102/66.1/12.2	[1]
SIO-03	7.11595	46.14895	760	Aiguilles Rouges Massif	/	/	4.6 $\pm$ 0.4	184/80.7/25.9	[1]
SIO-04	7.08645	46.12603	480	Aiguilles Rouges Massif	/	/	4.4 $\pm$ 0.5	102/76.1/34.3	[1]
MRP-012	7.04576	46.19298	1175	Aiguilles Rouges Massif	5.5 $\pm$ 0.4	13.90 $\pm$ 0.16	/	/	[4]
MRP-013	7.04197	46.18918	930	Aiguilles Rouges Massif	4.4 $\pm$ 0.3	13.32 $\pm$ 0.18	/	/	[4]
MRP-014	7.03862	46.18652	740	Aiguilles Rouges Massif	4.6 $\pm$ 0.4	13.59 $\pm$ 0.21	/	/	[4]
MRP-022	7.06062	46.1977	2055	Morcles Nappe	6.6 $\pm$ 0.7	14.26 $\pm$ 0.18	/	/	[4]
MRP-071	7.05488	46.19427	1675	Arpille Massif	5.9 $\pm$ 0.4	/	/	/	[4]
MRP-200	7.01489	46.18225	560	Aiguilles Rouges Massif	5.0 $\pm$ 0.3	13.80 $\pm$ 0.18	/	/	[4]
MRP-015	7.03428	46.18592	450	Aiguilles Rouges Massif	4.2 $\pm$ 0.3	14.08 $\pm$ 0.24	/	/	[4]
MRP-208	7.06969	46.12082	460	Arpille Massif	5.4 $\pm$ 0.5	13.67 $\pm$ 0.16	/	/	[4]
MWeil-1	7.0948	46.18104	2130	Dorénaz Syncline	6.2 $\pm$ 0.4	14.02 $\pm$ 0.18	/	/	[4]
MRP-021	7.06599	46.19988	2420	Morcles Nappe	8.9 $\pm$ 0.4	14.63 $\pm$ 0.13	/	/	[4]

<sup>a</sup>Sources are 1: *Valla et al.* [2011a]; 4: *Rahn* [1994]. Effective uranium concentration (eU), equivalent sphere radius (a), and U/Th ratio (UTh) are used for AHe age predictions using a radiation-damage model [*Gautheron et al.*, 2009].

VIS sampling profile (VIS area close to the town of Visp, Figure 1c) within the Aar massif (upper Rhône valley) and (2) an area for the SIO elevation profile (SIO area between the towns of Martigny and Sion, Figure 1b) covering the Aiguilles Rouges massif (~100 km downstream in the Rhône valley).

[15] For the VIS area (Table 1), we compile 6 apatite AHe ages from *Valla et al.* [2011a] and 11 AFT ages from *Reinecker et al.* [2008] and *Wagner et al.* [1977] (Figures 1c, 2b, and 2d). AHe ages range from 1.6 to 4.6 Ma (Figure 2d) and the age-elevation relationship suggests an apparent exhumation rate of  $0.9 \pm 0.2$  km Myr<sup>-1</sup> (Pearson correlation coefficient  $r = 0.74$ ). AFT data are spatially distributed within the studied area (Figure 1c) and have not been collected following an age-elevation sampling strategy; however, AFT ages ranging from ~3 to 8 Ma (Figure 2d) yield an apparent exhumation rate of  $0.5 \pm 0.1$  km Myr<sup>-1</sup> when plotted against elevation ( $r = 0.83$ ). First-order and one-dimensional interpretation of the VIS data thus suggests an increasing apparent exhumation rate around the Miocene-Pliocene transition (~4–5 Ma, Figure 2d).

[16] The SIO data (Table 2) combine 7 apatite AHe ages collected along an elevation profile (Figures 1b, 2a, and 2c) (see *Valla et al.* [2011a] for details) with 10 AFT ages [*Rahn*, 1994] mostly collected along a second elevation profile further downstream in the Rhône valley (Figure 1b). AHe and AFT ages overlap and range from ~4 to 8 Ma (Figure 2c). First-order and one-dimensional interpretation of the age-elevation relationships suggests apparent exhumation rates of  $0.6 \pm 0.2$  km Myr<sup>-1</sup> ( $r = 0.74$ ) and  $0.6 \pm 0.1$  km Myr<sup>-1</sup> ( $r = 0.76$ ) for AHe and AFT data, respectively. Most AFT ages are associated with track length measurements [*Rahn*, 1994]; mean track lengths (MTL) are positively correlated with elevation (Figure 2c), indicating that low-elevation samples may have spent more time in the AFT Partial Annealing Zone [e.g., *Gallagher et al.*, 1998]. Other studies [*Soom*, 1990; *Seward and Mancktelow*, 1994] have also reported isolated AFT ages within this area, mainly at low elevations along the Rhône valley; however, those localized AFT data are extremely young (~1 to 3 Ma) compared to our AHe ages and to the AFT data of *Rahn*

[1994]. Potential causes for these differences are either poor AFT counting statistics, because of very few counted grains for some samples of *Soom* [1990] and *Seward and Mancktelow* [1994], and/or potential local complications such as fluid circulation. We thus choose to only select AFT data of *Rahn* [1994] to (1) favor in our modeling strategy consistent thermochronology data sets along elevation profiles instead of isolated data and (2) avoid problems with non-concordant and possibly low-quality thermochronology ages.

[17] Qualitative interpretation of the two data sets suggests apparent differences in the late Miocene–Pliocene exhumation histories of the Aar (VIS area) and Aiguilles Rouges (SIO area) massifs. While AFT data are nearly similar and suggest late Neogene exhumation rates around 0.5–0.6 km Myr<sup>-1</sup>, AHe ages clearly differ, with much younger ages and a ~50% higher apparent exhumation rate for the VIS AHe data (Figures 2a and 2b). The VIS data show an apparent acceleration in exhumation rate by a factor of two between closure of the AFT and AHe systems that should have occurred during the Pliocene (~4–5 Ma, Figure 2d). In contrast, AFT and AHe ages overlap in the SIO region (Figure 2c), suggesting synchronous cooling (at ~0.6 km Myr<sup>-1</sup>) through both the AFT and AHe closure temperatures during the late Miocene/early Pliocene, in agreement with relatively long mean track lengths (Figure 2c) [*Rahn*, 1994]. Alternatively, a potential explanation for the apparent disagreement between the SIO and VIS AHe data may be the observed differences in apatite U-Th content (Tables 1 and 2). Effective U concentrations (eU) in these apatites range from ~30 to 90 ppm (Table 1) for VIS samples, whereas SIO samples show much higher eU of ~80 to 210 ppm (Table 2) and thus have potentially higher AHe closure temperatures because of the radiation damage effect on He retention (see section 3.1).

[18] In addition to low-temperature cooling ages, we also consider cooling histories for the VIS and SIO samples quantified from apatite <sup>4</sup>He/<sup>3</sup>He thermochronometry [*Valla et al.*, 2011a]. This method [*Shuster and Farley*, 2004, 2005] maps the radiogenic <sup>4</sup>He distribution within an apatite crystal using proton-induced <sup>3</sup>He production [*Shuster et al.*, 2004] and step-degassing experiments [*Shuster and Farley*,

2004, 2005]. It thus enables deriving quantitative constraints on the cooling history from  $\sim 90^\circ\text{C}$ , where  $^4\text{He}$  starts to accumulate within the apatite crystal, down to surface temperatures. Quantitative interpretation of apatite  $^4\text{He}/^3\text{He}$  data [Shuster and Farley, 2005] requires numerical modeling to identify the sets of time-temperature ( $t$ - $T$ ) histories that are consistent with the observed  $^4\text{He}/^3\text{He}$  distribution [Schildgen et al., 2010]. The model generates random  $t$ - $T$  histories and predicts an evolving spatial distribution of  $^4\text{He}$  for each cooling path, assuming a uniform spatial distribution of U and Th and an effective spherical diffusion geometry with surface/volume ratio equivalent to the analyzed grain [Schildgen et al., 2010]. For each randomly generated cooling history, the model first calculates a (U-Th)/He age that is compared to the measured age, using the RDAAM algorithm [Flowers et al., 2009] to take into account the radiation damage effects on He retention. If the predicted and measured ages are consistent, a model  $^4\text{He}/^3\text{He}$  ratio evolution is calculated using the same analytical heating schedule as the sample and compared to observed ratios [Shuster et al., 2005; Schildgen et al., 2010]. Here, we use cooling histories from VIS and SIO  $^4\text{He}/^3\text{He}$  data reported by Valla et al. [2011a]. First-order interpretation of  $t$ - $T$  histories qualitatively reveals rapid late Neogene cooling of both VIS and SIO samples from  $\geq 7$ –6 Ma until 5–4 Ma (see VIS-03, SIO-06, and SIO-07, Figures 7a, 8a, and 8b, respectively) and a final exhumation pulse around 1 Ma that is recorded only by low- and medium-elevation samples. Valla et al. [2011a] interpreted this recent exhumation as being linked to significant relief increase through glacial valley carving since  $\sim 1$  Ma. Here, we aim to provide tighter constraints on the timing and magnitude of this valley-carving event; we wish to obtain a precise quantification of both the timing and amount of local relief increase associated with Rhône valley deepening at both the VIS and SIO sampling sites. To achieve this, we performed forward thermal-kinematic modeling of the SIO and VIS areas using the full  $^4\text{He}/^3\text{He}$  data sets, in contrast to Valla et al. [2011a] who relied only on the contrast between high-elevation and valley-bottom samples to infer significant Pleistocene relief increase.

### 3.3. Modeling Approach

[19] We aim to quantitatively interpret low-temperature thermochronology data and  $^4\text{He}/^3\text{He}$ -derived cooling paths in terms of both denudation and relief histories. This requires defining denudation and relief scenarios (i.e., timing and rates for both denudation history and relief evolution) that we test by computing and comparing their predicted cooling histories, as outlined below. To this end, we use the thermal-kinematic model Pecube [Braun, 2003]. Our numerical approach and details about the thermal and geometric parameterization of the numerical problem are presented in detail in Appendix A and Table A1.

[20] We assume that rock exhumation is achieved by uniform block uplift. Although we previously pointed out the potential activity of the Rhône-Simplon fault during the late Neogene [e.g., Mancktelow, 1992; Reinecker et al., 2008; Campani et al., 2010], the main dip-slip strand of this fault is located outside our studied area, along the Simplon shear zone, and its activity is thought to have peaked before  $\sim 15$  Ma [Campani et al., 2010]. Thus, any uplift associated with fault movement is likely to be uniform over the SIO and

VIS study areas. Moreover, the thermochronology data from the VIS area (Figure 1c), which cross the fault zone, do not present significant age differences between the two sides of the Rhône valley (Figure 2d), suggesting that the vertical component of movement along the Rhône-Simplon fault in this area has been negligible during the late Neogene.

[21] Pecube enables numerical modeling of exhumation under either steady state or time-varying topography, and thus allows us to address the potential effects of transient topographic relief on crustal isotherms [Mancktelow and Grasemann, 1997; Foeken et al., 2007] and consequently on thermochronology data [Braun, 2002]. Relief evolution has been incorporated into Pecube following different approaches. Most recent studies have used the concept of the relief ratio between past and present-day topographies to address massif-scale relief changes [e.g., Herman et al., 2010b; Valla et al., 2010a; van der Beek et al., 2010; Glotzbach et al., 2011a], while Braun and van der Beek [2004] and Herman et al. [2010a] coupled Pecube with a surface process model to physically simulate topographic evolution. Here, we choose a different and simplified approach for predicting relief evolution in Pecube simulations. Valla et al. [2011a] deduced from the  $^4\text{He}/^3\text{He}$ -derived cooling contrast between high- and low-elevation samples, that relief has increased in the study area by efficient valley carving while peak elevations remained constant. We thus assume that the paleotopography is similar to the present-day topography except that valley bottoms are filled up to a specified elevation ( $H_{\text{limit}}$  (see section 4 for details)). The way we define relief evolution in Pecube remains fairly simplistic and does not capture the complexities of landscape evolution processes. Some limitations include the stable planform drainage pattern assumed in our numerical approach, and the geometric approach to relief evolution in which parts of the landscape above a given elevation are fixed to their present-day value and relief evolves through valley carving only. Although our approach might be stylized with respect to complex glacial and fluvial erosion processes, it allows us to follow a one parameter strategy (i.e.,  $H_{\text{limit}}$ ) to model relief evolution in Pecube simulations, resulting in improved computational efficiency and model simplicity (see our discussion in the following about model complexity).

[22] Inverse modeling has been performed using a recently developed approach [e.g., Braun and Robert, 2005; Herman et al., 2007, 2010a, 2010b; Valla et al., 2010a; van der Beek et al., 2010] combining the thermal-kinematic code Pecube [Braun, 2003] with the neighborhood algorithm (NA) inversion method [Sambridge, 1999a, 1999b] to (1) extract best fitting denudation and relief scenarios from thermochronology data (NA sampling stage) and (2) derive quantitative estimates of the precision with which denudation rates, timing and relief evolution are resolved (NA appraisal stage). The NA approach has been fully described in previous studies [Herman et al., 2010a; Valla et al., 2010a; Glotzbach et al., 2011a]; it is based on a misfit evaluation following the log likelihood function ( $\text{Ln}(L)$ ):

$$\text{Ln}(L) = -0.5 \sum_{i=1}^N \sum_{j=1}^M \frac{(\alpha_{j,\text{mod}} - \alpha_{j,\text{dat}})^2}{\sigma_j^2} \quad (1)$$

where  $N$  is the number of data sets (AFT, AHe, and/or MTL data),  $M$  is the number of samples in each data set (Tables 1

**Table 3.** VIS Inversions<sup>a</sup>

Inversion <sup>b</sup> (param./obs.)	$E_1$ (km Myr <sup>-1</sup> )	$T_{E1-2}$ (Ma)	$E_2$ (km Myr <sup>-1</sup> )	$T_{E2-3}$ (Ma)	$E_3$ (km Myr <sup>-1</sup> )	$T_R$ (Ma)	$H_{limit}$ (m)	Log Likelihood	BIC <sup>b</sup>
Range	0–4	1–10	0–4	1–10	0–4	1–14	600–3900	$Ln(L)$	
RunV1 (1/17)	0.8 ±0.01	-	-	-	-	-	-	-33.6	70
RunV2 (3/17)	3.9 ±0.7	9.0 +1.0/-2.8	0.7 ±0.01	-	-	-	-	-30.8	70.1
RunV3 (5/17)	3.9 +0.2/-0.4	7.9 ±0.6	0.4 ±0.1	-	-	2.1 ±0.8	2800 ±400	-21.4	56.9
RunV4 (5/17)	3.8 +0.3/-0.9	8.1 ±0.7	0.3 ±0.1	4.1 ±2.1	0.8 ±0.2	-	-	-24.8	63.7
RunV5 (7/17)	3.4 ±0.4	8.1 ±1.1	2.8 ±1.2	6.7 ±1.6	0.1 +0.5/-0.1	3.1 ±1.1	3400 ±400	-22.7	65.3
RunV3* (5/17)	3.4 +0.7/-1.5	9.9 +0.1/-1.7	0.5 ±0.2	-	-	1.2 +1.6/-0.2	3000 ±400	-21.5	57.2

<sup>a</sup>Bayesian estimates after the NA appraisal stage for parameters  $E_1, E_2, E_3, T_{E1-2}, T_{E2-3}, T_R$  and  $H_{limit}$  (optimal values (mode) and estimated uncertainties of parameters, see text for description and discussion).

<sup>b</sup>Each inversion is characterized by a number of free parameters to be inverted (param.) and a number of observations (obs., i.e., thermochronological data). Almost all inversions (RunV1 to RunV5) use the conventional He production-diffusion-ejection model [Wolf *et al.*, 1998; Meesters and Dunai, 2002] for AHe age predictions; inversion RunV3\* uses a radiation-damage model [Gautheron *et al.*, 2009].

and 2),  ${}^i\alpha_{j,mod}$  and  ${}^i\alpha_{j,dat}$  are predicted and observed values for AFT/AHe ages or MTL data, respectively, and  ${}^i\sigma_j$  is the uncertainty on the data. Further details about the NA inversion procedure are given in Appendix A.

[23] Estimating the complexity of the exhumation history from inverse numerical modeling requires defining complex denudation and relief scenarios. A major unknown in inverse theory is the appropriate dimensionality of the problem, or the number of model parameters inverted for, compared to the intrinsic resolution of the data [e.g., Akaike, 1974; Schwarz, 1978]. In our case, we have to define the number of denudation/relief phases in our model, i.e., the number of  $t$ - $T$  points in the cooling history to be constrained by the thermochronology data [e.g., Gallagher *et al.*, 2005; Glotzbach *et al.*, 2011a] and associated denudation rates, timing, and relief parameters. We thus need to find a balance between satisfactorily fitting the thermochronology data and over-interpreting them with too complex and unrealistic models. We use the Bayesian information criterion (BIC) [Schwarz, 1978] to assess the appropriate number of exhumation phases allowed by our data resolution:

$$BIC = -2Ln(L) + k \ln(n) \quad (2)$$

where  $k$  and  $n$  are the number of free parameters (denudation rates, timing and relief parameters) and observations (thermochronology data, i.e., AFT/AHe ages and MTL), respectively. The appropriate model will thus be defined by (1) best fitting exhumation scenarios matching the input thermochronology

data and (2) lowest BIC values, avoiding highly complex models [Glotzbach *et al.*, 2011a].

[24] We do not perform similar inverse modeling to interpret  ${}^4\text{He}/{}^3\text{He}$ -derived  $t$ - $T$  paths, but rather use forward thermal-kinematic modeling for computational efficiency. This approach does not require any numerical algorithms to predict thermochronology data from output thermal histories; we directly compare  $t$ - $T$  paths derived from the  ${}^4\text{He}/{}^3\text{He}$  data with Pecube outputs [e.g., Schildgen *et al.*, 2010]. We first put qualitative constraints on the late Neogene exhumation of VIS and SIO samples, especially on the timing of exhumation phases and associated rates, by first-order inspection of  ${}^4\text{He}/{}^3\text{He}$ -derived  $t$ - $T$  cooling paths. We then quantitatively assess the magnitude of relief development associated with the late stage exhumation pulse observed in the  ${}^4\text{He}/{}^3\text{He}$  data (i.e., late Pliocene to Pleistocene history) to gain further quantitative constraints on valley-deepening (previously estimated by Valla *et al.* [2011a]), as well as on the timing of this event. Our approach thus allows comparing outcomes on exhumation and relief scenarios from (1) the inverse models using AFT and AHe data and (2) forward modeling to constrain  ${}^4\text{He}/{}^3\text{He}$ -derived cooling histories.

## 4. Modeling Results

### 4.1. Inverse Modeling of Thermochronology Data

[25] For both the VIS and SIO data sets, we performed a set of inversions with various degrees of model complexity (i.e., number of inverted parameters, Tables 3 and 4). All

**Table 4.** SIO Inversions<sup>a</sup>

Inversion <sup>b</sup> (param./obs.)	$E_1$ (km Myr <sup>-1</sup> )	$T_{E1-2}$ (Ma)	$E_2$ (km Myr <sup>-1</sup> )	$T_{E2-3}$ (Ma)	$E_3$ (km Myr <sup>-1</sup> )	$T_R$ (Ma)	$H_{limit}$ (m)	Log Likelihood	BIC
Range	0–4	1–10	0n4	1–10	0–4	1–14	600–3900	$Ln(L)$	
RunS1 (1/26)	0.65 ±0.01	-	-	-	-	-	-	-86.7	176.7
RunS2 (3/26)	2.7 ±1.0	5.4 ±0.1	0.25 ±0.01	-	-	-	-	-62.8	135.4
RunS3 (5/26)	3.9 +0.1/-0.2	5.7 ±0.2	0.25 ±0.06	-	-	6.6 ±0.6	1600 ±500	-59.8	136.0
RunS4 (5/26)	2.6 ±0.4	5.8 ±3.4	0.1 +0.3/-0.1	4.5 +3.9/-3.5	0.15 ±0.06	-	-	-59.4	135.1
RunS5 (7/26)	3.9 +0.1/-0.4	6.3 ±0.4	0.9 ±0.2	3.8 ±0.4	0.1 +0.1/-0.1	8.3 ±1.5	2500 ±100	-56.5	135.8
RunS3* (5/26)	2.6 ±0.3	6.7 ±0.3	0.25 ±0.08	-	-	2.5 ±0.5	1500 ±400	-61.6	139.5
RunS5* (7/26)	2.5 ±0.9	5.8 ±1.0	1.0 +1.2/-1.0	4.5 ±1.1	0.1 +0.3/-0.1	6.0 ±2.8	1600 ±800	-60.4	143.6

<sup>a</sup>Bayesian estimates after the NA appraisal stage for parameters  $E_1, E_2, E_3, T_{E1-2}, T_{E2-3}, T_R$  and  $H_{limit}$  (optimal values (mode) and estimated uncertainties of parameters, see text for description and discussion).

<sup>b</sup>Each inversion is characterized by a number of free parameters to be inverted (param.) and a number of observations (obs., i.e., thermochronological data). Most inversions (RunS1 to RunS5) use the conventional He production-diffusion-ejection model [Wolf *et al.*, 1998; Meesters and Dunai, 2002] for AHe age predictions; inversions RunS3\* and RunS5\* use a radiation-damage model [Gautheron *et al.*, 2009].

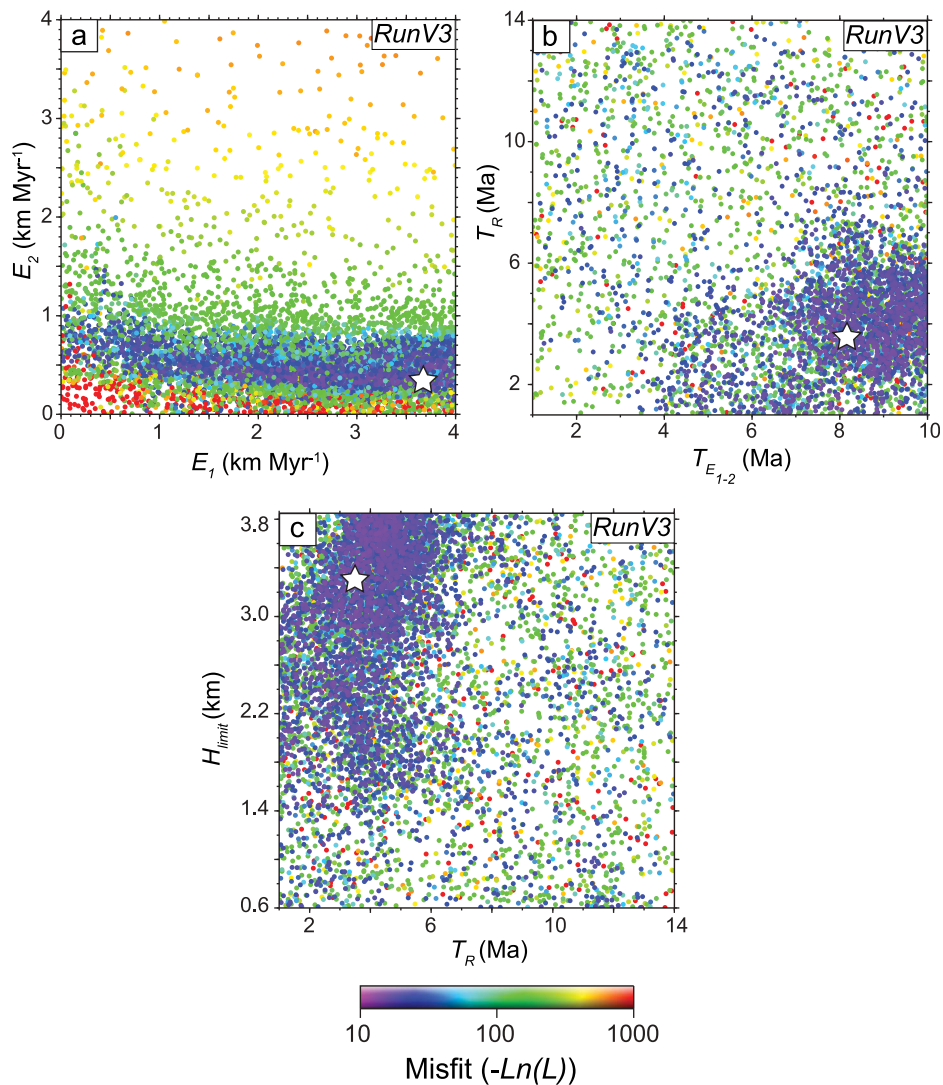


**Figure 3.** Scatterplots for most appropriate VIS inversion (RunV3, see Table 3 for details). Each dot corresponds to a forward model; its color is proportional to the misfit value between predictions and data ( $-\ln(L)$ ). Each diagram is the projection onto a plane defined by two of the five parameters. (a) Denudation rates  $E_1$  and  $E_2$ ; (b) denudation and relief transition times,  $T_{E1-2}$  and  $T_R$ , respectively; and (c) onset time of relief increase  $T_R$  and paleoelevation of valley bottom  $H_{limit}$ ; horizontal and vertical axes define the parameter space. White stars indicate the overall best fit model.

inversions are run over 15 Myr (i.e., 15 Ma to present). We define one, two and three phase denudation scenarios with associated denudation rates ( $E_1$ ,  $E_2$  and  $E_3$ , range: 0–4 km Myr<sup>-1</sup>) and transition times between each phase ( $T_{E1-2}$ ,  $T_{E2-3}$ , range: 1–10 Ma). Exhumation scenarios include either steady state or time-varying topography, with the onset of relief development  $T_R$  ranging between 1 and 14 Ma, and with paleovalley bottoms at higher elevation compared to present-day conditions, defined by the minimum paleovalley floor elevation ( $H_{limit}$ ).  $H_{limit}$  ranges are bounded by minimum and maximum elevations within the two modeled areas (600–3900 m and 400–3200 m for the VIS and SIO areas, respectively (Figures 1b and 1c)). All inverted parameters and their respective ranges are listed in Tables 3 and 4 for VIS and SIO inversions, respectively, together with the best fitting (maximum log likelihood) parameter values, resulting BIC values and associated

uncertainties. Inversion outputs are also visualized as scatterplots showing parameter combinations and associated model misfits from the NA sampling stage (Figures 3 and 5) and one-dimensional marginal probability density functions (pdfs) of individual parameter values after the NA appraisal stage (Figures 4 and 6). Below, we subsequently present inversion results for the VIS (RunV, models Table 3) and SIO data (RunS models, Table 4).

[26] For the VIS area, we performed three steady state topography inversions with either one (RunV1), two (RunV2) or three (RunV4) denudation phases. Inversion results (Table 3) show that we both maximize the likelihood ( $\ln(L)$  from  $-33.5$  to  $-24.8$ ) and optimize the BIC (from 70.0 to 63.7) by adding successive denudation phases. Inversions including time-varying topography (RunV3 and RunV5) led to better predictions ( $\ln(L) = -21.4$  and  $-22.7$ , respectively); BIC values show that the optimal exhumation

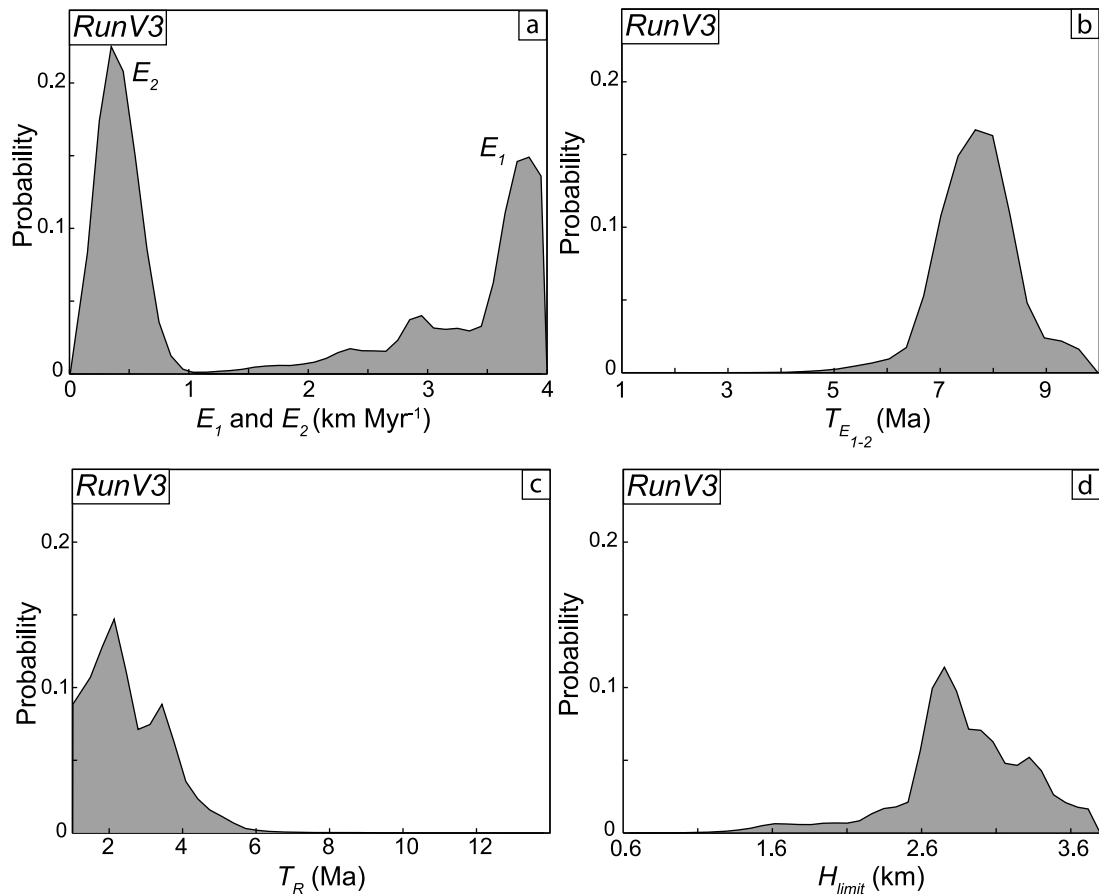


**Figure 4.** One-dimensional posterior probability density functions (pdfs) for most appropriate VIS inversion (RunV3, Figure 3 and Table 3) after the NA appraisal stage: (a) denudation rates  $E_1$  and  $E_2$ ; (b) denudation transition time  $T_{E1-2}$ ; (c) onset time of relief increase  $T_R$ ; and (d) paleoelevation of valley bottom  $H_{limit}$ . Horizontal axes define range of each parameter.

scenario combines two denudation phases with a phase of relief development (RunV3, BIC = 56.9,  $\sim 10\%$  lower than other BIC values); the three phase denudation scenario under evolving relief (RunV5) leads to a higher BIC value of 65.3. Output predictions for inversion RunV3 are reported as scatterplots in Figure 3 to allow first-order interpretation of the inversion results. Denudation rates during the second phase ( $E_2 \approx 0.2\text{--}0.8$  km Myr $^{-1}$ , Figure 3a) appear to be much tighter constrained than those of the first phase ( $E_1 \approx 1\text{--}4$  km Myr $^{-1}$ , Figure 3a); the transition between these two denudation phases may have occurred between 7 and 10 Ma ( $T_{E1-2}$ , Figure 3b). Timing estimates for relief development suggest a Pliocene initiation of valley incision ( $T_R \approx 2\text{--}6$  Ma, Figure 3c) and relief predictions set constraints on the paleovalley floor elevations between 2.0 and 3.9 km ( $H_{limit}$ , Figure 3c). The NA appraisal stage allows us to derive quantitative estimates on parameter values (Figure 4 and Table 3). One-dimensional marginal pdfs confirm that relatively high mean denudation rates ( $E_1 = 3.9 \pm 0.2\text{--}0.4$  km Myr $^{-1}$ , Figure 4a) are followed by moderate and better constrained mean denudation rates ( $E_2 = 0.4 \pm 0.1$  km Myr $^{-1}$ , Figure 4a). The transition time between the two denudation phases is also well constrained (Figure 4b) and must have occurred during the late Miocene ( $T_{E1-2} = 7.9 \pm 0.6$  Ma, Table 4). Timing predictions concerning relief

development are less tight (Figure 4c); however, they suggest a late Pliocene initiation of relief carving ( $T_R = 2.1 \pm 0.8$  Ma) and a paleovalley bottom at much higher elevations ( $H_{limit} = 2800 \pm 400$  m, Figure 4d) than at present (valley bottoms at  $\sim 600\text{--}800$  m elevation, Figure 1c).

[27] We previously reported relatively low to moderate eU concentrations for VIS samples ( $\sim 30\text{--}90$  ppm, Table 1). Here, we assess the influence of including radiation damage effects on the AHe age calculations and the resulting constraints on denudation and relief predictions. We thus perform a similar inversion to RunV3 with two denudation phases and relief development but using a radiation damage model [Gautheron *et al.*, 2009] to predict AHe ages (RunV3\*, Table 3). Inversion results provide similar log likelihood and BIC values ( $-21.4\text{--}21.5$  and  $56.9/57.2$  for RunV3 and RunV3\*, respectively (Table 3)). Optimal parameter values are also quite similar (Table 3), although, in detail, RunV3\* suggests lower ( $E_1 = 3.4 \pm 0.7\text{--}1.5$  km Myr $^{-1}$ ) and slightly higher ( $E_2 = 0.5 \pm 0.2$  km Myr $^{-1}$ ) rates for the first and second denudation phases, respectively, and a somewhat older transition between the two phases ( $T_{E1-2} = 9.9 \pm 0.1\text{--}1.7$  Ma). Relief predictions also differ somewhat, RunV3\* suggesting both younger ( $T_R = 1.2 \pm 1.6\text{--}0.2$  Ma) and stronger ( $H_{limit} = 3000 \pm 400$  m) valley carving (Table 3). However, all optimal parameter values overlap

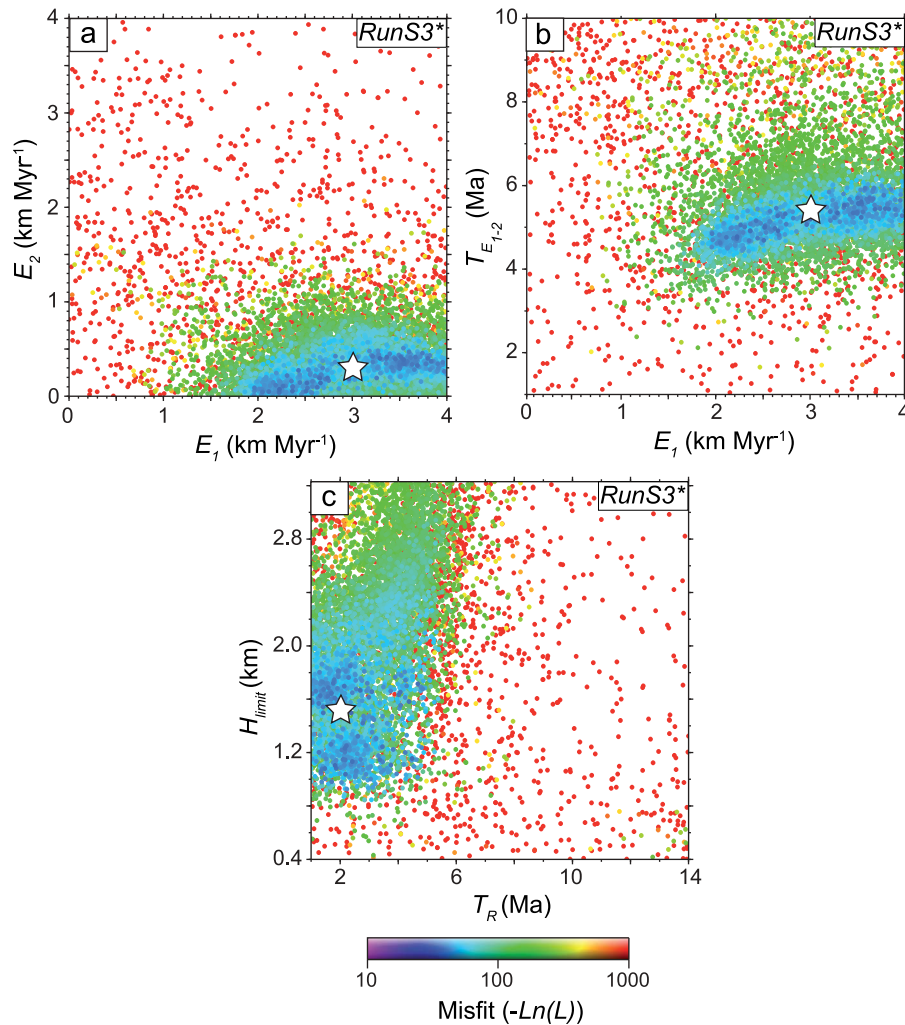


**Figure 5.** Scatterplots for most appropriate SIO inversion (RunS3\*, see Table 4 for details). Each dot corresponds to a forward model; its color is proportional to the misfit value between predictions and data ( $-\ln(L)$ ). Each diagram is the projection onto a plane defined by two of the five parameters. (a) Denudation rates  $E_1$  and  $E_2$ ; (b) denudation transition time and denudation rate during the first phase,  $T_{E_1-2}$  and  $E_1$ , respectively; and (c) onset time of relief increase  $T_R$  and paleoelevation of valley bottom  $H_{limit}$ ; horizontal and vertical axes define the parameter space. White stars indicate the best fitting model.

within their  $1\sigma$  uncertainty, indicating that radiation damage effects are not a major influence on the VIS AHe data, consistent with the moderate eU contents (Table 1).

[28] We adopt the same approach for SIO inversions (RunS, Table 4); however, output results clearly differ from RunV model predictions. Both log likelihood and BIC values are much higher ( $-86.7$  to  $-56.5$  and  $135.1$  to  $176.7$  for  $\ln(L)$  and BIC, respectively), and except for RunS1, which provided the highest BIC value ( $176.7$ ), all inversions yield very similar BIC estimates (between  $\sim 136$  and  $\sim 144$ ; less than 6% difference between all BIC values) so we cannot quantitatively assess which scenario best explains the SIO data. We interpret this somewhat disappointing outcome to be due to the strong overlap between AFT and AHe ages (Figure 2c) and the inability of the Pecube model to simultaneously predict the observed overlapping AFT and AHe ages, as well as the supplementary MTL data. Furthermore, using a radiation damage model to calculate AHe ages (RunS3\* and RunS5\*) does not clearly improve the

misfit to the observed data ( $\ln(L) \sim -60$  and BIC values  $\sim 140$ , Table 4).

[29] The SIO and VIS areas are geographically very close and are not separated by major tectonic structures (Figure 1); we can thus reasonably assume that their exhumation history, at least in terms of late Neogene exhumation phases, and their relief development are similar because of their common geomorphic setting along the Rhône valley. We consequently consider the scenario of two denudation phases with relief evolution used to interpret the VIS data as also being representative of the SIO exhumation history (RunS3 and RunS3\*, Table 4) to derive optimal estimates on denudation and relief parameters. We include the effect of radiation damage defects on AHe ages, as SIO samples present much higher eU concentrations ( $\sim 80$ – $210$  ppm, Table 2) than VIS samples. The main difference between the inversion including radiation damage effects (RunS3\*) and that using conventional He-diffusion kinetics (RunS3) concerns the prediction for the onset time of relief development ( $T_R$ );

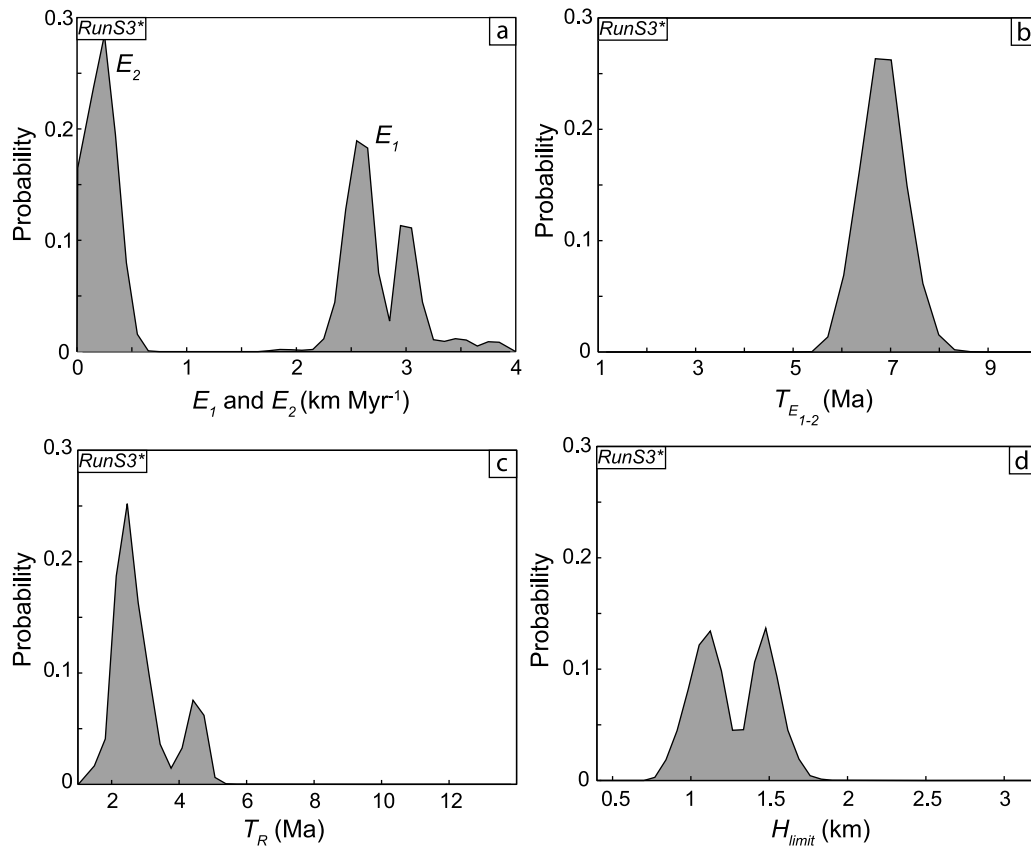


**Figure 6.** One-dimensional posterior pdfs for most appropriate SIO inversion (RunS3\*, Figure 5 and Table 4) after the NA appraisal stage: (a) denudation rates  $E_1$  and  $E_2$ ; (b) denudation transition time  $T_{E1-2}$ ; (c) onset time of relief increase  $T_R$ ; and (d) paleoelevation of valley bottom  $H_{limit}$ . Horizontal axes define range of each parameter.

although both inversions predict similar amplitudes of relief change ( $H_{limit} = 1600 \pm 500$  and  $1500 \pm 400$  m for RunS3 and RunS3\*, respectively (Table 4)). RunS3 suggests a late Miocene onset of valley carving ( $T_R = 6.6 \pm 0.6$  Ma, Table 4), while RunS3\* predicts a much later initiation, during the late Pliocene ( $T_R = 2.5 \pm 0.5$  Ma, Table 4 and Figure 6), in closer agreement with VIS predictions ( $T_R \approx 1.2$ – $2.1$  Ma, Table 3). This result highlights the importance of including radiation damage effects for AHe age predictions [Gautheron *et al.*, 2009] in Pecube simulations to best explain the SIO data (because of their higher eU values, Table 2).

[30] Results for inversion RunS3\* are reported in Figures 5 and 6. As previously discussed, this scenario has been chosen to match the preferred history predicted by the VIS inversions; however, parameter estimates are not guided by these earlier inversions yet lead to similar outcomes: a rapid denudation phase ( $E_1 \approx 2$ – $4$  km Myr $^{-1}$ , Figure 5a) until the Miocene-Pliocene transition ( $T_{E1-2} \approx 4$ – $6$  Ma, Figure 5b), followed by much lower denudation rates ( $E_2 \approx 0$ – $0.4$  km Myr $^{-1}$ , Figure 5a). Relief development predictions also suggest a Pliocene-Quaternary onset of valley carving for the SIO area ( $T_R \approx 1$ – $5$  Ma, Figure 5c) with a paleovalley bottom at  $\sim 1$ – $2$  km elevation (Figure 5c). One-dimensional pdfs (Figure 6) provide quantitative estimates for these parameters (Table 4). Similar to VIS results, the denudation rate of the most recent phase is tightly constrained ( $E_2 = 0.25 \pm$

$0.08$  km Myr $^{-1}$ , Figure 6a) while estimates for the initial denudation rate are less precise ( $E_1 = 2.6 \pm 0.4$  km Myr $^{-1}$ ; the pdf appears to be bimodal with peaks at  $\sim 2.5$  and  $\sim 3.0$  km Myr $^{-1}$  (Figure 6a)). The transition between the two denudation phases may have occurred in the late Miocene ( $T_{E1-2} = 6.7 \pm 0.3$  Ma, Figure 6b), in agreement with estimates for the VIS area ( $T_{E1-2} \approx 7$ – $10$  Ma, Table 4). Relief predictions are less constrained (Figures 6c and 6d) and suggest moderate valley carving ( $H_{limit} = 1500 \pm 400$  m; a bimodal pdf with peaks at  $\sim 1.1$  and  $\sim 1.5$  km (Figure 6d)) occurring in the late Pliocene–Pleistocene ( $T_R = 2.5 \pm 0.5$  Ma; a main peak in the pdf at  $\sim 2.5$  Ma and a minor peak at  $\sim 4.5$  Ma, illustrating the lesser resolution of SIO data in constraining relief evolution (Figure 6c)).

#### 4.2. Forward Modeling of $^4\text{He}/^3\text{He}$ Data

[31] We now present results of Pecube forward models aiming to further constrain the late Neogene and Pleistocene exhumation histories for the VIS and SIO samples from AHe and  $^4\text{He}/^3\text{He}$  data. We ran three phase exhumation scenarios over 15 Myr, in agreement with the above inversion outcomes, as well as sample cooling paths quantified from  $^4\text{He}/^3\text{He}$  data [Valla *et al.*, 2011a] (Figures 7 and 8). However, apatite  $^4\text{He}/^3\text{He}$  data only provide constraints on the cooling history since the onset of He retention (i.e., for temperatures below the AHe closure temperature [Shuster and Farley, 2005]). Therefore, constraints on late Miocene

exhumation (denudation rates and timing) cannot be precisely extracted from the  $^4\text{He}/^3\text{He}$  data, as most samples have AHe ages younger than  $\sim 5\text{--}6$  Ma (Figures 2a and 2b). First-order estimates for the late Miocene exhumation history are best provided by summit samples, which experienced only little cooling since the Pliocene (VIS-03, SIO-06, and SIO-07, Figures 7a, 8a, and 8b, respectively).

[32] The  $^4\text{He}/^3\text{He}$ -derived cooling paths for VIS-03 suggest rapid denudation (minimum estimates of  $\sim 1\text{--}1.5$  km  $\text{Myr}^{-1}$ ), which ended at  $\sim 3\text{--}4$  Ma (Figure 7a). Other VIS samples do not have sufficient resolution to constrain the late Neogene exhumation, although most suggest a deceleration in exhumation rates at around  $3\text{--}5$  Ma (Figure 7b–7e). We thus choose to impose an initial denudation phase at  $1.5$  km  $\text{Myr}^{-1}$  for our VIS models, ending at  $3.5$  Ma and followed by very slow denudation at  $0.001$  km  $\text{Myr}^{-1}$ . SIO samples have older AHe ages than the VIS samples (Figure 2a) and consequently provide more constraints on the late Neogene exhumation history. First-order interpretation of SIO cooling paths also reveals a rapid exhumation phase that ended at  $\sim 5\text{--}6$  Ma. Forward modeling for SIO-06 and SIO-07 (summit samples, Figures 8a and 8b) suggests rapid denudation (minimum estimates of  $\sim 0.75\text{--}1.5$  km  $\text{Myr}^{-1}$ ) until  $\sim 5.5\text{--}5$  Ma, followed by very little exhumation ( $\sim 0.001$  km  $\text{Myr}^{-1}$ ). In the following, we impose an initial denudation phase ( $1.0$  km  $\text{Myr}^{-1}$ ) ending at  $5$  Ma for SIO models.

[33] Figures 7 and 8 clearly show that medium- to low-elevation SIO and VIS samples record a late stage exhumation pulse at  $\sim 1\text{--}2$  Ma, in contrast to high-elevation samples that have remained at surface temperatures for the last  $3\text{--}5$  Myr. This contrast led *Valla et al.* [2011a] to interpret the late stage exhumation signal as reflecting major relief increase through Rhône valley carving, instead of a regional denudation pulse affecting the massifs. Note that these data, like all thermochronology data, only quantify exhumation histories; our data cannot evaluate potential (isostatic) peak uplift [e.g., *Small and Anderson*, 1998]. Here, we aim to quantitatively constrain the magnitude of this topographic change by using all available  $^4\text{He}/^3\text{He}$  data and focusing on the Rhône paleovalley floor changes required by both the VIS and SIO data. We test six different relief scenarios for the VIS samples (based on the amount of late stage cooling in the  $^4\text{He}/^3\text{He}$ -derived  $t\text{--}T$  paths), with paleovalley bottom elevations ( $H_{limit}$ ) ranging between  $1900$  and  $2400$  m (associated relief increase between  $\sim 80$  and  $105\%$ , Figure 7), and compare resulting  $t\text{--}T$  paths predicted by Pecube with those recorded by the  $^4\text{He}/^3\text{He}$  data. The summit sample (VIS-03) sets upper limits on the predicted relief development, excluding the  $105\%$  relief-increase scenario ( $H_{limit} = 2400$  m, Figure 7a), similar to VIS-06 results (Figure 7d). Medium-elevation samples (Figures 7b–7d) allow us to discard low relief-increase scenarios ( $\sim 80$  and  $85\%$  relief increase,  $H_{limit} = 1900\text{--}2000$  m). Finally, the valley bottom sample (VIS-07, Figure 7e) does not provide significant resolving power to decipher the magnitude of relief increase. In summary, we propose that the VIS paleovalley floor elevation may have been between  $2100$  and  $2300$  m before Rhône valley carving, resulting in a  $\sim 90\text{--}100\%$  increase in local relief (Figure 7).

[34] We adopt the same approach for SIO samples, with six paleorelief scenarios ranging between  $\sim 80$  and  $105\%$

relief increase ( $H_{limit} = 1400\text{--}1900$  m, Figure 8). The summit samples (SIO-06 and SIO-07) do not provide any constraint on the paleovalley floor elevation; all relief scenarios agree with the  $^4\text{He}/^3\text{He}$ -derived cooling paths (Figures 8a and 8b). Quantitative constraints on valley deepening primarily come from the medium- and low-elevation samples (Figures 8c and 8d); both SIO-02 and SIO-04 exclude the lowest-amplitude relief change ( $\sim 80\%$  relief increase,  $H_{limit} = 1400$  m) while SIO-04 discards the  $105\%$  relief-increase scenario ( $H_{limit} = 1900$  m, Figure 8d). Paleovalley floor predictions from SIO samples thus suggest a  $\sim 85\text{--}100\%$  increase in local relief ( $H_{limit} = 1500\text{--}1800$  m).

[35] Finally, although *Valla et al.* [2011a] have provided evidence for a late stage exhumation pulse triggered by relief development since  $\sim 1$  Ma, they did not fully investigate the timing of this event. Here, we aim to derive more precise constraints on the timing of relief increase from the  $^4\text{He}/^3\text{He}$  data, by using previously determined relief scenarios ( $H_{limit} = 2200$  and  $1650$  m for the VIS and SIO areas, respectively) and varying the onset of valley carving between  $0.5$  and  $2.5$  Ma. We only use valley bottom samples (VIS-07 and SIO-04) as we expect those to have best recorded the timing of the late stage exhumation pulse. The results show that, although we cannot discriminate between most recent scenarios ( $0.5\text{--}1.5$  Ma), an onset of final exhumation  $\geq 2$  Ma predicts a poorer match to the  $^4\text{He}/^3\text{He}$  cooling paths (Figure 9). We thus propose that the late stage exhumation pulse triggered by local relief increase initiated at  $1.0 \pm 0.5$  Ma (Figure 9).

## 5. Discussion

### 5.1. Exhumation and Relief Histories From Thermochronology Data

[36] We have derived quantitative constraints on both exhumation and relief histories using thermochronology and numerical thermal-kinematic modeling. We show that performing both inverse modeling [e.g., *Valla et al.*, 2010a] of AFT and AHe data combined with quantitative interpretation of  $^4\text{He}/^3\text{He}$  cooling paths [*Shuster et al.*, 2005; *Schildgen et al.*, 2010; *Valla et al.*, 2011a] provides complementary constraints on the denudation and relief histories of the studied areas. On the one hand, inverse modeling of AFT and AHe data constrains late Miocene and Pliocene exhumation of the VIS and SIO areas by providing quantitative estimates on denudation rates and timing of changes in these rates, and to a lesser extent on the relief history. On the other hand, forward modeling designed to match the  $t\text{--}T$  histories inferred from  $^4\text{He}/^3\text{He}$  data provides tight constraints on late stage exhumation through valley carving.

[37] Inverse models produce contrasted results for both areas, with statistically better constrained exhumation scenarios for the VIS samples, implying a two phase denudation history and a significant recent relief increase (Table 3 and Figures 3 and 4). SIO data do not provide such well-constrained results, and inverse modeling does not allow discriminating between the different exhumation scenarios (Table 4). We thus choose a similar denudation history (two phase denudation scenario with a phase of relief change) for both the VIS and SIO areas as they are geographically very close. Moreover, the relief histories for both areas must have been tightly connected as they encompass the same major

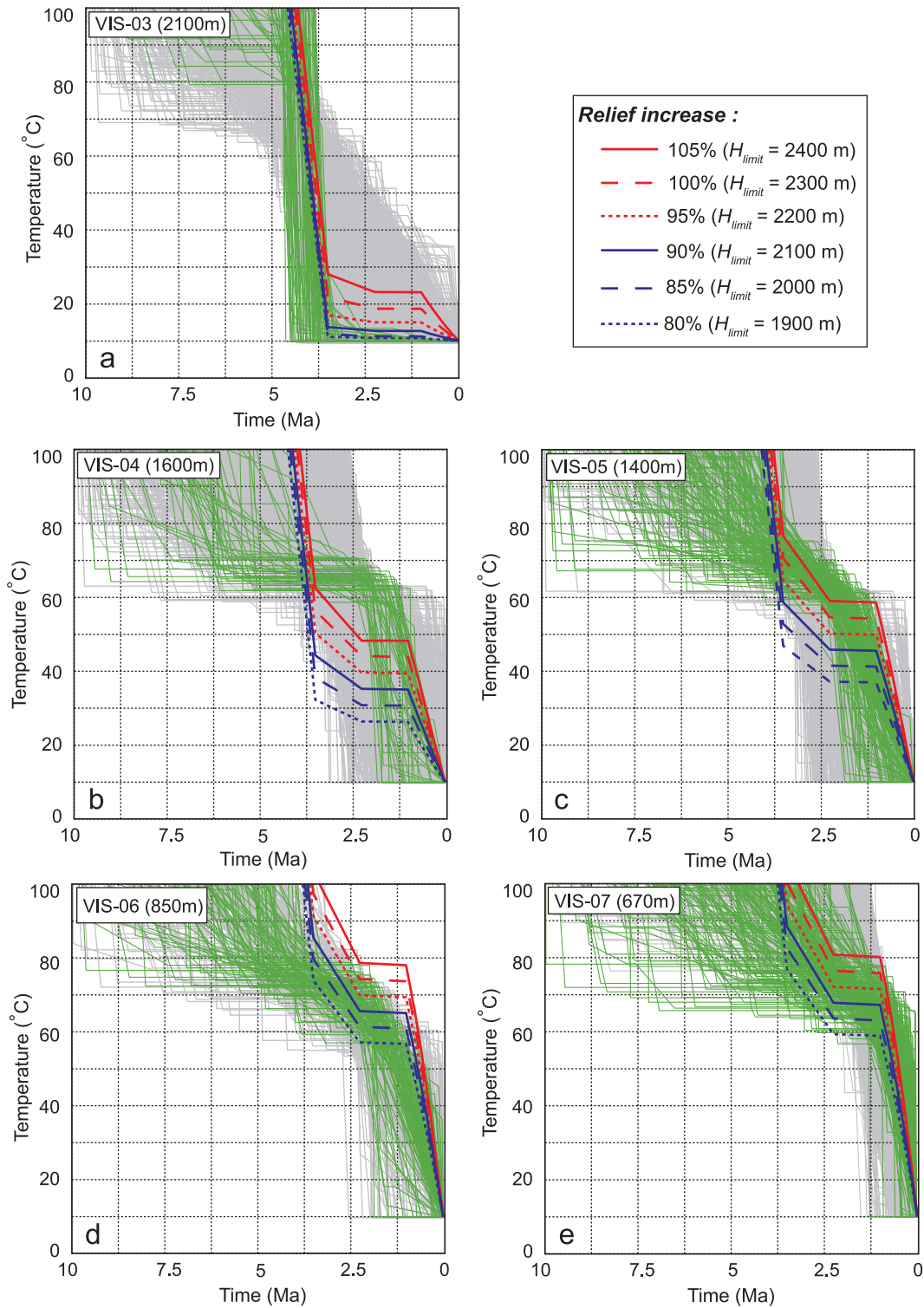


**Figure 7.** Cooling paths for VIS samples inferred from  $^4\text{He}/^3\text{He}$  thermochronometry and Pecube models (see Figures 1 and 2 for sample locations). Green and gray lines show good and acceptable cooling paths, respectively, from  $^4\text{He}/^3\text{He}$  data for (a) VIS-03, (b) VIS-04, (c) VIS-05, (d) VIS-06, and (e) VIS-07 [Valla et al., 2011a]. Thick blue and red lines show Pecube-modeled cooling paths simulating relief carving of various amplitudes (80 to 105% relief increase; see legend for color code) since  $\sim 1$  Ma. See text for other parameters.

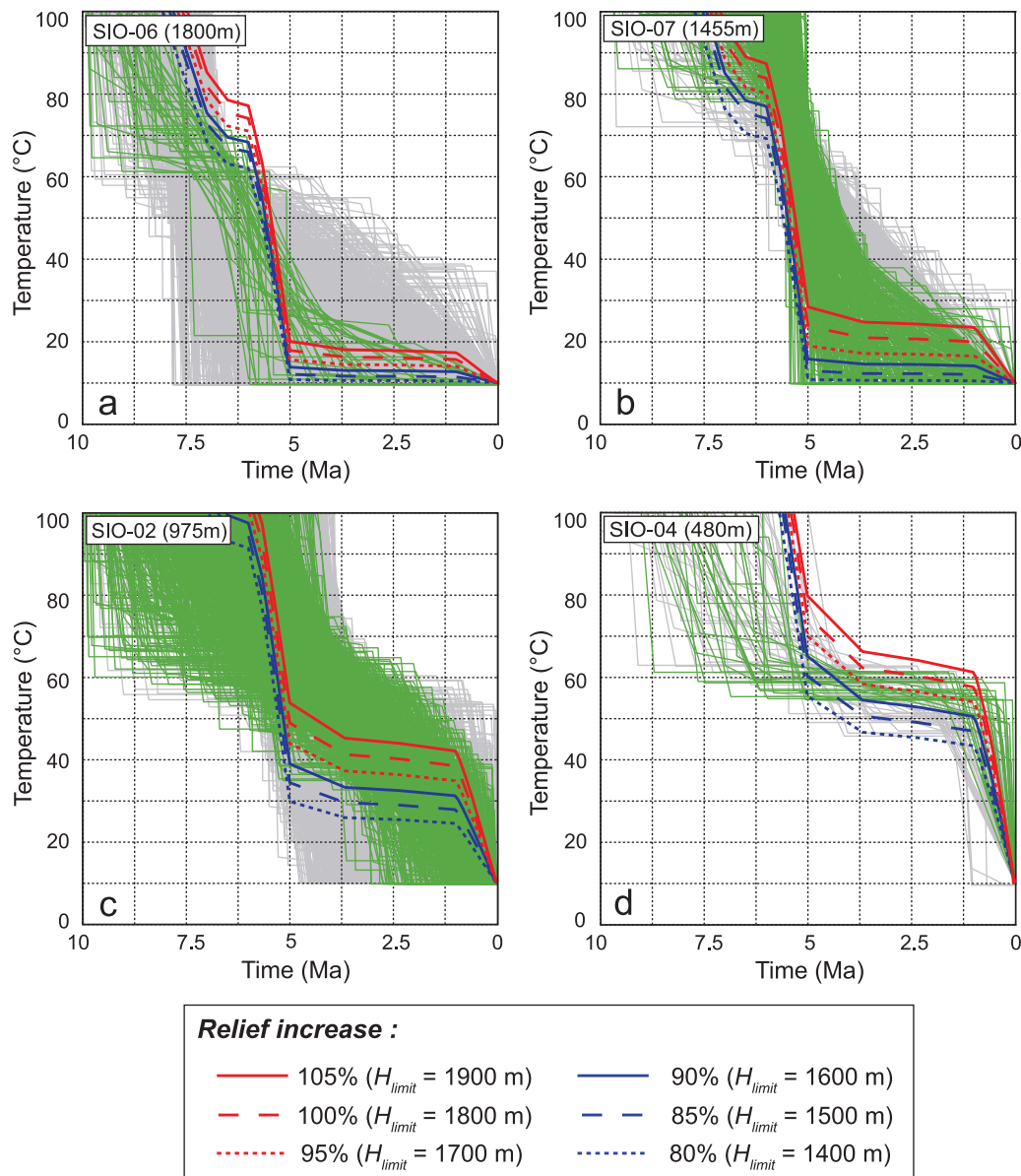


**Figure 8.** Cooling paths for SIO samples inferred from  $^4\text{He}/^3\text{He}$  thermochronometry and Pecube models (see Figures 1 and 2 for sample locations). Green and gray lines show good and acceptable cooling paths, respectively, from  $^4\text{He}/^3\text{He}$  data for SIO-06 (a), (b) SIO-07, (c) SIO-02, and (d) SIO-04 [Valla *et al.*, 2011a]. Thick blue and red lines show Pecube-modeled cooling paths simulating relief carving of various amplitudes (80 to 100% relief increase; see legend for color code) since  $\sim 1$  Ma. See text for other parameters.

valley (i.e., the Rhône valley, Figure 1). We also suggest that using a statistical information criterion (BIC) [Schwarz, 1978] may allow quantitative assessment of the adequate complexity of the inverse model [e.g., Gallagher *et al.*, 2005; Glotzbach *et al.*, 2011a]; however, small (<10%) differences in the BIC values, as in our case for the SIO data, do not permit to define an appropriate exhumation scenario without external constraints from adjacent areas (in this case the VIS data).

[38] Differences between SIO and VIS model results may be partly due to the spatial distribution of thermochronology data (Figures 1b and 1c). AHe and AFT data from the SIO area are distributed along two separate profiles (Figure 1b), while VIS data are more broadly distributed (especially the

AFT data, Figure 1c). These results are in close agreement with findings of Valla *et al.* [2011b], which suggest that sampling along age-elevation profiles only may not be the most appropriate way to infer both exhumation and relief histories. Another potential explanation, previously proposed in section 4.1, is the overlap between AFT and AHe ages for SIO samples and the inclusion of supplementary MTL data (Figure 2c), preventing the NA inverse model to converge toward best fitting exhumation scenarios that simultaneously match the observed AHe, AFT and MTL data. Potential local variations in geothermal gradient, associated with fluid circulation within the SIO area [Sonney and Vuattaz, 2009], although difficult to quantify and

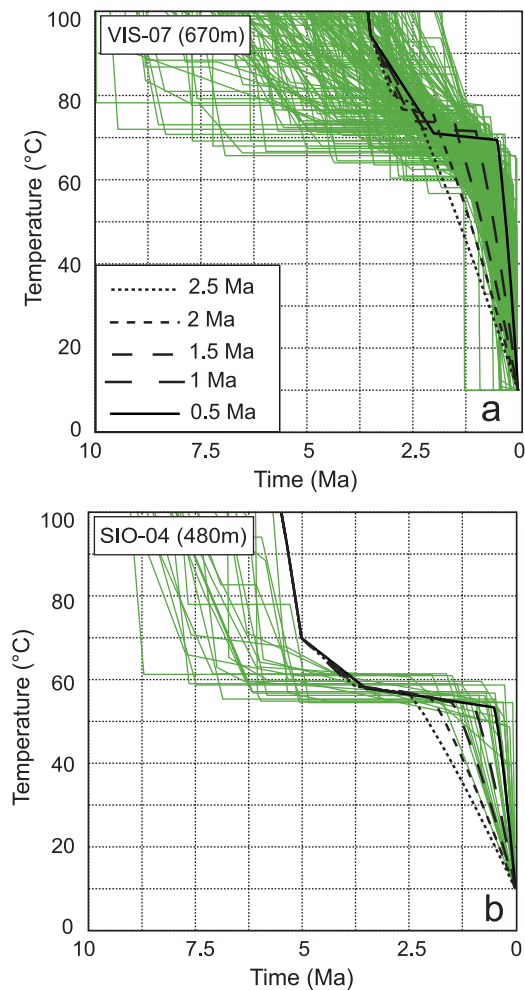


**Figure 9.** Timing of late stage valley carving from VIS and SIO valley bottom samples. Green lines show cooling paths fitting the  $^4\text{He}/^3\text{He}$  data for samples (a) VIS-07 and (b) SIO-04; black lines represent Pecube-modeled cooling histories simulating relief increase initiating between 0.5 and 2.5 Ma (see text for details).

include in thermal-kinematic modeling, could have a significant influence on thermochronometric ages [e.g., *Whipp and Ehlers, 2007*] and may partly explain the overlap between observed AFT and AHe ages.

[39] We have used both a conventional He-diffusion model and a model that takes into account radiation damage effects on apatite He retention [*Gautheron et al., 2009*] to predict AHe ages. We show that including radiation damage effects does not make a significant difference for VIS predictions; however, output results for SIO samples are clearly influenced by radiation damage effects because of their higher eU contents (Table 2). Although this model helps to improve the BIC contrast between different exhumation scenarios (RunS3\* compared to RunS3, Table 4), we still have to rely on VIS modeling outputs to constrain the SIO exhumation history. Our modeling results also highlight that, even though SIO samples have AHe ages ranging between 4 and 8 Ma (Table 2) and have experienced rapid recent cooling, they have such high eU content (>100 ppm, Table 2) that radiation damage effects must be incorporated

into their numerical interpretation [*Shuster et al., 2006; Flowers et al., 2009; Gautheron et al., 2009*].

[40] In the following, we first interpret our modeling results for the late Miocene and Pliocene exhumation of both the VIS and SIO areas, and then discuss the implications of our outcomes on late stage deepening of the Rhône valley in terms of Pleistocene landscape evolution and geomorphic process response to glacial/interglacial oscillations.

## 5.2. Late Miocene–Pliocene Exhumation of the Aar and Aiguilles Rouges Massifs

[41] VIS inverse modeling results imply a two phase denudation history (RunV3 and RunV3\*, Table 3), with relatively rapid denudation rates ( $\sim 2\text{--}4 \text{ km Myr}^{-1}$ , Table 3) until 8–10 Ma followed by moderate denudation rates of  $\sim 0.4\text{--}0.5 \text{ km Myr}^{-1}$ . Inferred Pliocene denudation rates are similar to those inferred by previous thermochronology studies in the adjacent Aar and Gotthard areas [*Reinecker et al., 2008; Vernon et al., 2009; Glotzbach et al., 2010; Campani et al., 2010*], which all predicted denudation rates of  $\sim 0.3\text{--}0.5 \text{ km Myr}^{-1}$  for late Miocene to Pliocene times. Moreover, a late Neogene exhumation pulse ( $\sim 1\text{--}2 \text{ km Myr}^{-1}$ ) lasting until  $\sim 5\text{--}6 \text{ Ma}$  has been suggested for the Mont Blanc [*Glotzbach et al., 2011a*] and the Ecrins-Pelvoux [*van der Beek et al., 2010*] massifs. *Vernon et al.* [2009] and *Glotzbach et al.* [2010] also pointed out a phase of rapid exhumation between  $\sim 10$  and 7 Ma for the Aar and Gotthard massifs, respectively, although they report lower denudation rates ( $\sim 0.7 \text{ km Myr}^{-1}$ ) than our inverse modeling results ( $\sim 2\text{--}4 \text{ km Myr}^{-1}$ , Table 3). Most of our thermochronological ages from the VIS profile (Table 1 and Figure 2d) are younger than this exhumation event and thus cannot provide tight constraint on this exhumation period; thus predicted denudation estimates have to be interpreted with caution. Although we choose, for computational simplicity, not to incorporate ZFT data into our thermal-kinematic modeling, ZFT ages close to the VIS area show partial to total Alpine resetting, with most ZFT ages between  $\sim 10$  and 12 Ma [*Soom, 1990; Glotzbach et al., 2010*], and would limit the duration of this exhumation pulse to  $\sim 2\text{--}5 \text{ Ma}$  (i.e., maximum of  $\sim 10 \text{ km}$  exhumation). We thus propose that our predicted denudation rates from inverse modeling could be overestimated as we did not include higher temperature constraints for this 15–8 Ma time window. Constraining the early denudation history of the area would have required including high-temperature data in our modeling strategy, as in the Ecrins-Pelvoux [*van der Beek et al., 2010*] or Mont Blanc [*Glotzbach et al., 2011a*] massifs. However, in general, our results are consistent with other studies [*Vernon et al., 2009; Glotzbach et al., 2010*] in suggesting a transition from rapid to moderate denudation rates at  $\sim 8\text{--}10 \text{ Ma}$ .

[42] VIS AHe ages alone (Figure 2d), as well as  $^4\text{He}/^3\text{He}$  data, are too young to have recorded the late Neogene exhumation pulse; however, they suggest a different Pliocene denudation history than our inverse modeling. One-dimensional AHe age-elevation relationship suggests relatively rapid apparent exhumation rates ( $\sim 0.9 \text{ km Myr}^{-1}$ , Figure 2d) between 2 and 4 Ma, in agreement with  $^4\text{He}/^3\text{He}$ -derived  $t\text{--}T$  paths from the VIS summit sample ( $\sim 1\text{--}1.5 \text{ km Myr}^{-1}$  until  $\sim 3\text{--}4 \text{ Ma}$ , followed by very little exhumation, Figure 7a). We previously explained that  $^4\text{He}/^3\text{He}$  data may not have sufficient resolution to quantitatively constrain the late

Miocene to early Pliocene exhumation history; however, this Pliocene exhumation pulse (recorded by both AHe and  $^4\text{He}/^3\text{He}$  data but not evidenced by our numerical inverse modeling) may potentially result from a short denudation event [Reinecker et al., 2008; Pignalosa et al., 2011] that cannot be easily extracted from low-temperature thermochronology ages alone, but clearly appears in the  $^4\text{He}/^3\text{He}$  data. This short event could have been smeared out in the inversion to overall moderate exhumation rates ( $\sim 0.4$  km  $\text{Myr}^{-1}$ , Table 3) over the late Neogene.

[43] Inverse modeling results for SIO are in closer agreement with  $^4\text{He}/^3\text{He}$  cooling paths for late Miocene and Pliocene times. Model RunS3\* (Table 4) reveals rapid late Miocene denudation ( $\sim 2.5$  km  $\text{Myr}^{-1}$ , Figures 5 and 6) until  $\sim 6$ – $7$  Ma (somewhat later than for the Aar massif, but not significantly different), followed by moderate denudation rates during the Pliocene ( $\sim 0.25$  km  $\text{Myr}^{-1}$ , Figures 5 and 6); while  $^4\text{He}/^3\text{He}$  data (Figure 8) suggest quite lower denudation rates ( $\sim 0.75$ – $1.5$  km  $\text{Myr}^{-1}$ ) until 5–5.5 Ma followed by very little exhumation. In summary, even though timing and rates may differ slightly (potentially because of smearing of denudation rate predictions through the inverse approach), both inverse modeling results and  $^4\text{He}/^3\text{He}$  data evidence rapid late Miocene denudation followed by lower denudation rates during the Pliocene, in agreement with inverse-modeling predictions for the exhumation history of the adjacent Mont Blanc massif [Glotzbach et al., 2011a]. Rahn [1994] also reported ZFT ages of  $\sim 100$  Ma that reveal only partial Alpine resetting, implying that the Miocene exhumation history has been different from that inferred in the VIS area, and suggesting that our predicted denudation rates from inverse modeling could not have been sustained for more than 3 to 4 Ma during the late Miocene.

[44] This late Miocene decrease in exhumation rates has now been reported from most of the ECMs [Bigot-Cormier et al., 2006; Glotzbach et al., 2008; Vernon et al., 2009; Glotzbach et al., 2010; van der Beek et al., 2010; Glotzbach et al., 2011a]. Different explanations have been proposed to explain it, such as a global climate change at the end of the Messinian [e.g., Willett et al., 2006] and/or potential regional tectonic controls (e.g., lowering of Alpine convergence rates [Schmid et al., 1996]). However, this decrease in overall exhumation rates around the Miocene-Pliocene transition is not easily reconciled with the  $\sim 5$  Ma onset of exhumation in the north Alpine foreland basin [Cederbom et al., 2004, 2011] and increase in sediment flux [Kuhlemann et al., 2002] that have been interpreted as potentially reflecting an increase in erosional efficiency within the Alpine orogen [Willett et al., 2006]. One alternative explanation, recently proposed by Glotzbach et al. [2011a], connects the observed drop in the exhumation rates of the ECMs to widespread late Miocene exposure of crystalline basement rocks. Basement lithologies are less erodible than the overlying Mesozoic sedimentary cover units, but are better preserved in the sedimentary record, thus potentially reconciling the decrease in denudation rates with the observed sedimentation pulse at  $\sim 5$  Ma [Kuhlemann et al., 2002].

### 5.3. Pleistocene Relief Development and Implications for Landscape Evolution

[45] Our forward modeling results, and their comparison to  $^4\text{He}/^3\text{He}$ -derived cooling paths, clearly confirm that final

exhumation of SIO and VIS samples is caused by recent relief increase through valley carving [Valla et al., 2011a]. We have used the  $^4\text{He}/^3\text{He}$ -derived  $t$ - $T$  paths together with numerical thermal-kinematic modeling to place quantitative constraints on the preglacial Rhône valley floor elevation:  $2200 \pm 100$  m (VIS, Figure 7) and  $1650 \pm 150$  m (SIO, Figure 8), implying a  $\sim 85$ – $100\%$  increase in local relief during the last  $1.0 \pm 0.5$  Ma (Figure 9). As discussed before, the quoted elevations might slightly overestimate the true paleoelevations as our models do not take into account the isostatic rebound in response to valley carving.

[46] Our inverse modeling results (based on AFT and AHe data) also provided quantitative predictions for late Pliocene relief development. VIS modeling results (Table 3) suggest that paleovalley floor elevations may have been at  $\sim 2700 \pm 400$  m elevation (i.e., a larger relief increase compared to  $^4\text{He}/^3\text{He}$  predictions), and predict an onset of valley carving between  $\sim 1$  and 3 Ma (RunV3 and RunV3\* inversions, Table 3). SIO relief predictions (RunS3\*, Table 4) confirm  $^4\text{He}/^3\text{He}$  estimates of paleovalley floor elevation ( $1500 \pm 400$  m, Figure 6d) and provide similar timing constraints as the VIS data ( $\sim 2$ – $3$  Ma, Figure 6c). As previously explained, inverse modeling of AFT and AHe thermochronologic ages does not provide as much resolution on the late stage exhumation as the  $^4\text{He}/^3\text{He}$  data, consequently leading to less precise timing and relief-growth estimates [see also Valla et al., 2010a, 2011b]. However, even though the timing and rate predictions differ slightly (i.e., overestimated relief-increase and timing inferences, associated with larger uncertainties), inverse modeling results are in overall agreement with  $^4\text{He}/^3\text{He}$  cooling  $t$ - $T$  paths; both suggest that the topographic relief of the Rhône valley has roughly doubled since  $\sim 1$ – $2$  Ma.

[47] Thermochronologic studies from adjacent areas report a significant increase in exhumation rates (up to  $\sim 1$  km  $\text{Myr}^{-1}$ ) since  $\sim 2$ – $3$  Ma [Glotzbach et al., 2008, 2010; Campani et al., 2010; Pignalosa et al., 2011]; however, these studies did not interpret this exhumation pulse as being linked to relief development but rather to enhanced massif-scale denudation. Glotzbach et al. [2011a] managed to extract relief information by performing inverse modeling of thermochronology data from the Mont Blanc massif. Their results suggest an approximate doubling in topographic relief since  $\sim 1$ – $2$  Ma, in close agreement with our relief estimates from both inverse modeling and  $^4\text{He}/^3\text{He}$  data. Relief predictions from our thermochronology data are also consistent with  $\sim 1$  km of incision of the Aar valley, dated at  $\sim 0.8$ – $1.0$  Ma from cosmogenic burial dating of cave sediments [Haeuselmann et al., 2007].

[48] Both the existing literature data and our own results thus point toward a significant impact of Pleistocene glaciations on topographic relief growth in the European Alps [e.g., Valla et al., 2011a]. However, our timing predictions suggest that relief development within the core of the Alpine orogen postdated both the onset of the Northern Hemisphere glaciations at  $\sim 3.5$ – $2.7$  Ma [Haug et al., 2005; Lisiecki and Raymo, 2005; Mudelsee and Raymo, 2005] and evidence of late Pliocene glaciers within the European Alps [Schlüchter, 1986; Jeannin, 1991; Zuccoli, 2000]. We thus speculate, following Haeuselmann et al. [2007] and Valla et al. [2011a], that major valley carving within the Swiss Alps may be linked to the mid-Pleistocene climate transition from 41 kyr to 100 kyr glacial/interglacial oscillations [e.g.,

Lisiecki, 2010] and the onset of major and widespread Alpine glaciations [Muttoni et al., 2003]. Our results thus suggest, as also reported for the St. Elias Mountains in southern Alaska [e.g., Berger et al., 2008], that the mid-Pleistocene global establishment of strong periodic oscillations between glacial and interglacial conditions acted as a climatic threshold for geomorphic processes and promoted transient landscapes [Norton et al., 2010]. The result was strong Alpine relief development from mid-Pleistocene to present-day times, inducing an isostatic response to Quaternary erosional unloading [Molnar and England, 1990; Champagnac et al., 2007, 2008; van der Beek and Bourbon, 2008] that partly contributes to modern rock uplift [Schlatter et al., 2005].

[49] Our interpretation of significant relief development in the European Alps since mid-Pleistocene times differs from other mountainous environments such as Fiordland in the South Island of New Zealand [Shuster et al., 2011] and the Sierra Nevada in California [Brocklehurst and Whipple, 2002], where Pleistocene glaciations appear to have mainly led to a decrease in mean elevation and topographic relief by promoting erosion in high-elevation parts of the landscape. We speculate that these differences may be due to the preglacial establishment of major longitudinal valleys such as the Rhône Valley in the European Alps [e.g., Kühni and Pfiffner, 2001b], which during glacial times hosted massive and strongly erosive ice streams that rapidly deepened them. Such very large valleys are absent in both Fiordland and the Sierra Nevada, thus inhibiting funneling of major ice streams. Our results also differ from findings in the Southern Alps of New Zealand, where topographic relief appears to remain stable during glacial/interglacial cycles [Herman et al., 2010b]. The major difference in this case lies in the tectonic activity; whereas this is moderate to absent in the European Alps, very active tectonic and exhumation processes in the Southern Alps allow erosion of nearly the complete relief of the mountain belt within a single glacial/interglacial cycle. Whereas in the latter case tectonics may completely overwhelm any climatic signal, their particular tectonic and drainage evolution appear to render the European Alps very sensitive to late Cenozoic climate changes.

## 6. Conclusions

[50] On the basis of thermal-kinematic modeling of both low-temperature thermochronology ages and  $^4\text{He}/^3\text{He}$ -derived cooling paths, we derive quantitative constraints on the late Neogene and Quaternary exhumation and relief history of the Aar and Aiguilles Rouges massifs (Swiss Alps). Modeling results highlight the respective resolution of AFT/AHe data and  $^4\text{He}/^3\text{He}$  thermochronometry in quantifying both the denudation history and relief development. Inverse modeling of AFT and AHe data reveals that numerically interpreting thermochronology data first requires assessing the appropriate model complexity, as well as constraining thermal parameters using high-temperature thermochronometers and/or external constraints. Moreover, our results highlight the potential problem of interpreting AHe ages without taking into account the effects of radiation damage on apatite He retention even in relatively young samples that cooled rapidly but are characterized by high eU

content. We use two different numerical codes [Flowers et al., 2009; Gautheron et al., 2009] to include these effects in AHe age predictions; our results show that, for our study, both codes provide similar outcomes. Modeling results suggest a late Miocene exhumation pulse until  $\sim 5$ – $8$  Ma, consistent with recent thermochronological data from adjacent areas and the exhumation histories inferred for other ECMs. This exhumation event is followed by moderate ( $\sim <0.1$ – $0.5$  km Myr $^{-1}$ ) and apparently steady denudation rates during the Pliocene, contrasting with the inferred  $\sim 5$  Ma increase in sediment flux out of the orogen.

[51] Extracting relief information from thermochronological observations has remained elusive and age-elevation sampling strategies do not necessarily provide precise estimates of relief development. However, we have shown that using spatially distributed samples may help to provide quantitative information on topographic relief changes, although the best predictions are given by methods that are sensitive to lower temperatures, such as  $^4\text{He}/^3\text{He}$  thermochronometry. Our modeling results, in agreement with other thermochronological studies, provide evidence for a significant ( $\sim 100\%$ ) recent increase in local topographic relief. Moreover, we provide here precise quantification of the amount of Rhône valley carving ( $\sim 1$ – $1.5$  km) as well as the timing of its onset (0.5 to 1.5 Ma). We postulate this significant massif-scale relief change to have been triggered by the mid-Pleistocene climate transition and the resulting enhancement of transient landscape conditions by large-amplitude glacial/interglacial oscillations.

## Appendix A: Thermal-Kinematic Modeling and Inversion Method

[52] In this study, we employ the 3D finite element code Pecube [Braun, 2003], which solves the heat transfer equation [Carslaw and Jaeger, 1959] to determine the 3-D thermal structure within an exhuming crustal block:

$$\rho c \left( \frac{\partial T}{\partial t} + E \frac{\partial T}{\partial z} \right) = \frac{\partial}{\partial x} k \frac{\partial T}{\partial x} + \frac{\partial}{\partial y} k \frac{\partial T}{\partial y} + \frac{\partial}{\partial z} k \frac{\partial T}{\partial z} + H \quad (\text{A1})$$

where  $T(x, y, z, t)$  is the time-varying thermal field ( $^{\circ}\text{C}$ ),  $\rho$  is rock density ( $\text{kg m}^{-3}$ ),  $c$  is heat capacity ( $\text{J kg}^{-1} \text{K}^{-1}$ ),  $k$  is rock conductivity ( $\text{W m}^{-1} \text{K}^{-1}$ ),  $E$  is the vertical velocity of rocks with respect to the base of the model ( $\text{m yr}^{-1}$ , i.e., the rock-uplift rate, which is equal to the exhumation rate for steady state topography [England and Molnar, 1990; Willett and Brandon, 2002]), and  $H$  is the crustal radioactive heat production ( $\text{W m}^{-3}$ ).

[53] We use a priori information from geophysical studies [e.g., Stampfli et al., 1998; Tesauro et al., 2008] to fix the crustal thickness at 40 km (lower boundary of the crustal block, Table A1) and the basal crustal temperature at  $600^{\circ}\text{C}$  [e.g., Bousquet et al., 1997], in agreement with Moho temperature estimates of  $500$ – $800^{\circ}\text{C}$  [Viganò and Martin, 2007]. Estimates for the geothermal gradient [e.g., Vuattaz et al., 1993; Bianchetti, 1994; Sonney and Vuattaz, 2009; Pignalosa et al., 2011] suggest strong spatial variations along the Rhône valley and within the neighboring massifs, with mean values between  $20$  and  $>40^{\circ}\text{C km}^{-1}$ . Constraining both thermal parameters (i.e., the geothermal gradient or the

**Table A1.** Thermal-Kinematic and Elastic Parameters Used in Pecube<sup>a</sup>

Parameter	Value
Grid resolution (m)	750
Crustal thickness (km)	40
Crustal density (kg m <sup>-3</sup> )	2700
Sublithospheric mantle density (kg m <sup>-3</sup> )	3200
Young's modulus (Pa)	1.1011
Poisson ratio	0.25
Equivalent elastic thickness (km)	25
Thermal diffusivity (km <sup>2</sup> Myr <sup>-1</sup> )	25
Basal crustal temperature (°C)	600
Crustal heat production (μW m <sup>-3</sup> )	0.8 (2.1)
Sea level temperature (°C)	10

<sup>a</sup>See Appendix A for details. Crustal thickness is based on *Tesauro et al.* [2008]; basal crustal temperature is based on Moho temperature estimates [*Viganò and Martin*, 2007] and previous thermochronology studies in the European Alps [*Vernon et al.*, 2009; *van der Beek et al.*, 2010; *Glotzbach et al.*, 2011a]. Following *Vernon et al.* [2009] and *van der Beek et al.* [2010], crustal heat production has been set to obtain a geothermal gradient of ~25°C km<sup>-1</sup> during numerical inversions (~35°C km<sup>-1</sup> for forward models simulating <sup>4</sup>He/<sup>3</sup>He-derived cooling paths, following *Valla et al.* [2011a], see value in brackets). Thermal parameters (thermal conductivity, diffusivity, and crustal heat production) are within ranges observed from geophysical studies in the central European Alps [*Rybach et al.*, 1977; *Finckh*, 1981]. Poisson ratio, Young's modulus, and equivalent elastic thickness [e.g., *Pfiffner et al.*, 2002] are used for calculating the isostatic rebound in response to relief change [*Braun and Robert*, 2005].

basal crustal temperature) and the exhumation history from thermochronology data requires both low- and high-temperature thermochronometers [*Glotzbach et al.*, 2011a], which is beyond the scope of the present study. As we only use low-temperature thermochronology data (AFT, MTL and AHe data) in the present study, we thus choose to fix thermal parameters during the numerical inversions based on previous thermochronology studies in neighboring areas [*Vernon et al.*, 2009; *van der Beek et al.*, 2010; *Glotzbach et al.*, 2011a]. *Vernon et al.* [2009] and *van der Beek et al.* [2010] have proposed a fixed geothermal gradient of ~20–25°C km<sup>-1</sup>, although *Glotzbach et al.* [2011a] proposed higher values of ~30–40°C km<sup>-1</sup>. Preliminary tests reveal that, in our case, varying the geothermal gradient between ~25 and 35°C km<sup>-1</sup> does not significantly influence the inversion predictions. We thus decide to fix the initial geothermal gradient to 25°C km<sup>-1</sup> (Table A1) for inverse modeling of AFT and AHe thermochronology data. Surface temperatures are computed using a mean sea level temperature of 10°C and a lapse rate of 6°C km<sup>-1</sup> (Table A1). We adopted a slightly different approach to interpret *t*-*T* histories from <sup>4</sup>He/<sup>3</sup>He data using forward thermal-kinematic modeling to follow the previous work of *Valla et al.* [2011a], who arbitrarily fixed the present-day surface temperature to the modern mean surface temperature of the area for all samples (~10°C), and set a ~35°C km<sup>-1</sup> geothermal gradient for interpreting VIS and SIO cooling histories (Table A1). Following their study, we adopt similar thermal parameters for forward Pecube models and comparison with <sup>4</sup>He/<sup>3</sup>He-derived cooling histories (Table A1). Finally, imposed spatially uniform rock uplift is combined with additional isostatic uplift simulating the flexural response to erosional unloading associated with relief evolution [*Braun and Robert*, 2005]. Uplift is assumed to be completely

balanced by erosion. Following many studies aiming to constrain flexural parameters for the European Alps [*Stewart and Watts*, 1997; *Burkhard and Sommaruga*, 1998; *Pfiffner et al.*, 2002], we choose an equivalent elastic thickness of 25 km (Table A1) to simulate isostatic rebound [*van der Beek et al.*, 2010].

[54] Thermochronological ages are predicted from thermal histories using different numerical algorithms [e.g., *Braun*, 2003]. AFT ages and associated mean track lengths (MTL) are calculated using a forward model for AFT annealing [*Green et al.*, 1989; *Stephenson et al.*, 2006]. We choose this approach rather than more elaborate models taking variable annealing kinetics into account [e.g., *Ketcham*, 2005] because no kinetic indicators are available for most of the literature AFT data [*Wagner et al.*, 1977; *Rahn*, 1994; *Reinecker et al.*, 2008]. AHe ages are computed using a simple forward model for He production-diffusion-ejection [*Wolf et al.*, 1998; *Meesters and Dunai*, 2002]. However, as previously explained, radiation damage defects caused by α decay of U and Th [e.g., *Shuster et al.*, 2006] may influence the AHe closure temperature, potentially explaining the AHe age differences observed between the VIS and SIO profiles (Figure 2). Previous studies in the European Alps that interpreted thermochronology data using numerical modeling [*Vernon et al.*, 2009; *van der Beek et al.*, 2010; *Glotzbach et al.*, 2011a] did not consider this effect and only used conventional diffusion kinetics [*Wolf et al.*, 1998; *Meesters and Dunai*, 2002] for AHe age predictions, assuming that both low eU contents and relatively rapid cooling during Neogene exhumation of the external crystalline massifs limits the influence of radiation damage on AHe ages [e.g., *Glotzbach et al.*, 2011a]. Although our samples may also have been exhumed quite rapidly during the Neogene Alpine history, we want to assess the potential differences in denudation and relief predictions when considering the radiation damage effect on AHe ages (section 3.1), especially for the SIO samples with high eU concentration (80–210 ppm, Table 2). We therefore included the radiation damage model of *Gautheron et al.* [2009] in Pecube and use this alternative model besides the conventional kinetics to predict AHe ages.

[55] The NA comprises a two stage inversion approach: the first stage (NA sampling stage [*Sambridge*, 1999a]) iteratively explores the multidimensional parameter space to find optimal parameter combinations that minimize the misfit function. The multidimensional space is divided into Voronoi cells, each of them being sampled for forward Pecube modeling to construct misfit surfaces following the log likelihood function ( $\ln(L)$ , see equation (1) in main text). The calculated misfit surface is then used to concentrate subsequent sampling of the parameter space and ensures numerical convergence toward an optimal set of parameters. As explained in detail by *Glotzbach et al.* [2011a], the NA sampling stage is mainly controlled by three parameters: (1) the number of iterative samplings of the parameter space, (2) the number of forward Pecube models generated at each iteration, and (3) the number of Voronoi cells resampled after each misfit surface calculation. In this study, we perform ~8500 models for each inversion distributed in 55 iterations, with 95% resampling at each iteration, implying a rather broad search within the parameter space.

[56] The second stage (NA appraisal stage) uses the ensemble of generated models from the sampling stage to derive Bayesian estimates, i.e., posterior marginal probability density functions (pdf), of parameter values from the likelihood function defined above [Sambridge, 1999b]. Modeling results are represented both as scatterplots for different parameter combinations (NA sampling stage) and 1-D marginal pdfs of individual parameters (NA appraisal stage).

[57] **Acknowledgments.** This study is supported by INSU-CNRS through the European Science Foundation Eurocores Topo-Europe program 07-TOPO-EUROPE-FP-023 “Coupled climatic/tectonic forcing of European topography revealed through thermochronometry (Thermo-Europe)” (to P.A.v.d.B.), the Agence Nationale de la Recherche project ANR-08-BLAN-0303-01 “Erosion and Relief Development in the Western Alps” (to P.A.v.d.B.), U.S. National Science Foundation grant EAR-0720225 (to D.L.S.), the ANR-06-JCJC-0079 (to C.G.), and the Ann and Gordon Getty Foundation. It forms part of P.V.’s Ph.D. project at Université Joseph Fourier, supported by the French Ministry for Research and Higher Education. We thank M. Rahn, who kindly shared his unpublished fission track data, and S. Brocklehurst, B. Flowers, F. Schlunegger, and J. Spotila for very constructive and insightful comments. Computations were performed on Brutus, the high-performance computing facilities at ETH Zurich. The codes are available at <http://svn-geo.ethz.ch> after registering at this site.

## References

- Abrecht, J. (1994), Geologic units of the Aar massif and their pre-Alpine rock associations: A critical review, *Schweiz. Mineral. Petrogr. Mitt.*, **74**, 5–27.
- Akaike, H. (1974), A new look at the statistical identification model, *IEEE Trans. Autom. Control*, **19**, 716–723, doi:10.1109/TAC.1974.1100705.
- Barletta, V. R., C. Ferrari, G. Diolaiuti, T. Carmielli, R. Sabadini, and C. Smiraglia (2006), Glacier shrinkage and modeled uplift of the Alps, *Geophys. Res. Lett.*, **33**, L14307, doi:10.1029/2006GL026490.
- Beaumont, C., P. Fullsack, and J. Hamilton (1992), Erosional control of active compressional orogens, in *Thrust Tectonics*, edited by K. R. McClay, pp. 1–18, Chapman and Hall, London, doi:10.1007/978-94-011-3066-0\_1.
- Becker, A. (2000), The Jura Mountains—An active foreland fold-and-thrust belt?, *Tectonophysics*, **321**, 381–406, doi:10.1016/S0040-1951(00)00089-5.
- Berger, A. L., et al. (2008), Quaternary tectonic response to intensified glacial erosion in an orogenic wedge, *Nat. Geosci.*, **1**, 793–799, doi:10.1038/ngeo334.
- Bernet, M. (2009), A field-based estimate of the zircon fission-track closure temperature, *Chem. Geol.*, **259**, 181–189, doi:10.1016/j.chemgeo.2008.10.043.
- Bernet, M., M. Zattin, J. I. Garver, M. T. Brandon, and J. A. Vance (2001), Steady-state exhumation of the European Alps, *Geology*, **29**, 35–38, doi:10.1130/0091-7613(2001)029<0035:SSEOTE>2.0.CO;2.
- Bernet, M., M. Brandon, J. Garver, M. L. Balestieri, B. Ventura, and M. Zattin (2009), Exhuming the Alps through time: Clues from detrital zircon fission-track thermochronology, *Basin Res.*, **21**, 781–798, doi:10.1111/j.1365-2117.2009.00400.x.
- Bianchetti, G. (1994), Hydrogéologie et géothermie de la région de Lavey-les-Bains (Vallée du Rhône, Suisse), *Bull. Cent. Hydrogeol. Univ. Neuchatel*, **13**, 3–32.
- Bigot-Cormier, F., M. Sosson, G. Poupeau, J.-F. Stéphan, and E. Labrin (2006), The denudation history of the Argentera Alpine External Crystalline Massif (Western Alps, France-Italy): An overview from the analysis of fission tracks in apatites and zircons, *Geodin. Acta*, **19**, 455–473, doi:10.3166/ga.19.455-473.
- Bousquet, R., B. Goffé, P. Henry, X. Le Pichon, and C. Chopin (1997), Kinematic, thermal and petrological model of the central Alps: Lepontine metamorphism in the upper crust and eclogitisation of the lower crust, *Tectonophysics*, **273**, 105–127, doi:10.1016/S0040-1951(96)00290-9.
- Brandon, M. T., M. Roden-Tice, and J. I. Garver (1998), Late Cenozoic exhumation of the Cascadia accretionary wedge in the Olympic Mountains, northwest Washington State, *Geol. Soc. Am. Bull.*, **110**, 985–1009, doi:10.1130/0016-7606(1998)110<0985:LCEOTC>2.3.CO;2.
- Braun, J. (2002), Quantifying the effect of recent relief changes on age-elevation relationships, *Earth Planet. Sci. Lett.*, **200**, 331–343, doi:10.1016/S0012-821X(02)00638-6.
- Braun, J. (2003), Pecube: A new finite element code to solve the heat transport equation in three dimensions in the Earth’s crust including the effects of a time-varying, finite amplitude surface topography, *Comput. Geosci.*, **29**, 787–794, doi:10.1016/S0098-3004(03)00052-9.
- Braun, J., and X. Robert (2005), Constraints on the rate of post-orogenic erosional decay from low-temperature thermochronological data: Application to the Dabie Shan, China, *Earth Surf. Processes Landforms*, **30**, 1203–1225, doi:10.1002/esp.1271.
- Braun, J., and P. A. van der Beek (2004), Evolution of passive margin escarpments: What can we learn from low-temperature thermochronology?, *J. Geophys. Res.*, **109**, F04009, doi:10.1029/2004JF000147.
- Brocklehurst, S. H., and K. X. Whipple (2002), Glacial erosion and relief production in the Eastern Sierra Nevada, California, *Geomorphology*, **42**, 1–24, doi:10.1016/S0169-555X(01)00069-1.
- Burkhard, M., and A. Sommaruga (1998), Evolution of the western Swiss Molasse basin: Structural relations with the Alps and the Jura belt, in *Cenozoic Foreland Basins of Western Europe*, edited by A. Mascle et al., *Geol. Soc. Spec. Publ.*, **134**, 279–298.
- Calais, E., J.-M. Nocquet, F. Jouanne, and M. Tardy (2002), Current strain regime in the Western Alps from continuous Global Positioning System measurements, 1996–2001, *Geology*, **30**, 651–654, doi:10.1130/0091-7613(2002)030<0651:CSRTW>2.0.CO;2.
- Campani, M., F. Herman, and N. Mancktelow (2010), Two- and three-dimensional thermal modeling of a low-angle detachment: Exhumation history of the Simplon Fault Zone, central Alps, *J. Geophys. Res.*, **115**, B10420, doi:10.1029/2009JB007036.
- Carlsaw, H. S., and C. J. Jaeger (1959), *Conduction of Heat in Solids*, 3rd ed., 510 pp., Clarendon, Oxford, U. K.
- Cederbom, C., H. Sinclair, F. Schlunegger, and M. Rahn (2004), Climate-induced rebound and exhumation of the European Alps, *Geology*, **32**, 709–712, doi:10.1130/G20491.1.
- Cederbom, C. E., P. A. van der Beek, F. Schlunegger, H. D. Sinclair, and O. Oncken (2011), Rapid extensive erosion of the North Alpine foreland basin at 5–4 Ma, *Basin Res.*, **23**, 528–550, doi:10.1111/j.1365-2117.2011.00501.x.
- Champagnac, J.-D., C. Sue, B. Delacou, and M. Burkhard (2004), Brittle deformation in the inner NW Alps: From early orogen-parallel extrusion to late orogen-perpendicular collapse, *Terra Nova*, **16**, 232–242, doi:10.1111/j.1365-3121.2004.00555.x.
- Champagnac, J.-D., P. Molnar, R. S. Anderson, C. Sue, and B. Delacou (2007), Quaternary erosion-induced isostatic rebound in the Western Alps, *Geology*, **35**, 195–198, doi:10.1130/G23053A.1.
- Champagnac, J.-D., P. van der Beek, G. Diraison, and S. Dauphin (2008), Flexural isostatic response of the Alps to increased Quaternary erosion recorded by foreland basin remnants, SE France, *Terra Nova*, **20**, 213–220, doi:10.1111/j.1365-3121.2008.00809.x.
- Champagnac, J.-D., F. Schlunegger, K. Norton, F. von Blanckenburg, L. M. Abbühl, and M. Schwab (2009), Erosion-driven uplift of the modern central Alps, *Tectonophysics*, **474**, 236–249, doi:10.1016/j.tecto.2009.02.024.
- Delunel, R., D. Hantz, R. Braucher, D. L. Bourlès, P. Schoeneich, and J. Déparis (2010), Surface exposure dating and geophysical prospecting of the Holocene Lauvitel rock slide (French Alps), *Landslides*, **7**, 393–400, doi:10.1007/s10346-010-0221-0.
- Driscoll, N. W., and G. H. Haug (1998), A short circuit in thermohaline circulation: A cause for Northern Hemisphere glaciation?, *Science*, **282**, 436–438, doi:10.1126/science.282.5388.436.
- England, P., and P. Molnar (1990), Surface uplift, uplift of rocks, and exhumation of rocks, *Geology*, **18**, 1173–1177, doi:10.1130/0091-7613(1990)018<1173:SUUORA>2.3.CO;2.
- Farley, K. A. (2000), Helium diffusion from apatite: General behavior as illustrated by Durango fluorapatite, *J. Geophys. Res.*, **105**, 2903–2914, doi:10.1029/1999JB900348.
- Farley, K. A. (2002), (U-Th)/He dating: Techniques, calibrations, and applications, in *Noble Gases in Geochemistry and Cosmochemistry*, *Rev. Mineral. Geochem.*, vol. 47, edited by D. Porcelli, C. J. Ballentine, and R. Wieler, pp. 819–844, Mineral. Soc. of Am., Washington, D. C.
- Finckh, P. (1981), Heat-flow measurements in 17 perialpine lakes, *Geol. Soc. Am. Bull.*, **92**, 452–514, doi:10.1130/0016-7606(1981)92<108:HMPLS>2.0.CO;2.
- Finckh, P., and W. Frei (1991), Seismic reflection profiling in the Swiss Rhone valley, Part 1: Seismic reflection field work, seismic processing and seismic results of the Roche-Vouvry and Turttmann and Agam lines, *Eclogae Geol. Helv.*, **84**, 345–357.
- Flowers, R. M., R. A. Ketcham, D. L. Shuster, and K. A. Farley (2009), Apatite (U-Th)/He thermochronometry using a radiation damage accumulation and annealing model, *Geochim. Cosmochim. Acta*, **73**, 2347–2365, doi:10.1016/j.gca.2009.01.015.
- Foeken, J. P. T., C. Persano, F. M. Stuart, and M. ter Vooorde (2007), Role of topography in isotherm perturbation: Apatite (U-Th)/He and fission track results from the Malta tunnel, Tauern Window, Austria, *Tectonics*, **26**, TC3006, doi:10.1029/2006TC002049.
- Frey, M., and R. Ferreiro Maehlmann (1999), Alpine metamorphism of the central Alps, *Schweiz. Mineral. Petrogr. Mitt.*, **79**, 135–154.

- Gallagher, K., R. Brown, and C. Johnson (1998), Fission track analysis and its applications to geological problems, *Annu. Rev. Earth Planet. Sci.*, *26*, 519–572, doi:10.1146/annurev.earth.26.1.519.
- Gallagher, K., J. Stephenson, R. Brown, C. Holmes, and P. Fitzgerald (2005), Low temperature thermochronology and modeling strategies for multiple samples 1: Vertical profiles, *Earth Planet. Sci. Lett.*, *237*, 193–208, doi:10.1016/j.epsl.2005.06.025.
- Gautheron, C., and L. Tassan-Got (2010), A Monte Carlo approach to diffusion applied to noble gas/helium thermochronology, *Chem. Geol.*, *273*, 212–224, doi:10.1016/j.chemgeo.2010.02.023.
- Gautheron, C., L. Tassan-Got, J. Barbarand, and M. Pagel (2009), Effect of alpha-damage annealing on apatite (U-Th)/He thermochronology, *Chem. Geol.*, *266*, 157–170, doi:10.1016/j.chemgeo.2009.06.001.
- Glotsbach, C., J. Reinecker, M. Danisik, M. Rahn, W. Frisch, and C. Spiegel (2008), Neogene exhumation history of the Mont Blanc massif, Western Alps, *Tectonics*, *27*, TC4011, doi:10.1029/2008TC002257.
- Glotsbach, C., J. Reinecker, M. Danisik, M. Rahn, W. Frisch, and C. Spiegel (2010), Thermal history of the central Gotthard and Aar massifs (European Alps): Evidence for steady state, long-term exhumation, *J. Geophys. Res.*, *115*, F03017, doi:10.1029/2009JF001304.
- Glotsbach, C., P. A. van der Beek, and C. Spiegel (2011a), Episodic exhumation of the Mont Blanc massif, Western Alps: Constraints from numerical modelling of thermochronology data, *Earth Planet. Sci. Lett.*, *304*, 417–430, doi:10.1016/j.epsl.2011.02.020.
- Glotsbach, C., M. Bernet, and P. A. van der Beek (2011b), Detrital thermochronology records changing source areas and steady exhumation in the western European Alps, *Geology*, *39*, 239–242, doi:10.1130/G31757.1.
- Green, P. F., I. R. Duddy, G. M. Laslett, K. A. Hegarty, A. J. W. Gleadow, and J. F. Lovering (1989), Thermal annealing of fission tracks in apatite 4. Quantitative modelling techniques and extension to geological time-scales, *Chem. Geol.*, *79*, 155–182.
- Gudmundsson, G. H. (1994), An order of magnitude estimate of the current uplift rates in Switzerland caused by the Würm alpine deglaciation, *Eclogae Geol. Helv.*, *87*, 545–557.
- Hauselmann, P., D. E. Granger, P.-Y. Jeannin, and S.-E. Lauritzen (2007), Abrupt glacial valley incision at 0.8 Ma dated from cave deposits in Switzerland, *Geology*, *35*, 143–146, doi:10.1130/G23094A.
- Haug, G. H., et al. (2005), North Pacific seasonality and the glaciation of North America 2.7 million years ago, *Nature*, *433*, 821–825, doi:10.1038/nature03332.
- Hay, W. W., J. L. Sloan, and C. N. Wold (1988), Mass/age distribution and composition of sediments on the ocean floor and the global rate of sediment subduction, *J. Geophys. Res.*, *93*, 14,933–14,940, doi:10.1029/JB093iB12p14933.
- Herman, F., J. Braun, and W. Dunlap (2007), Tectonomorphic scenarios in the Southern Alps of New Zealand, *J. Geophys. Res.*, *112*, B04201, doi:10.1029/2004JB003472.
- Herman, F., et al. (2010a), Exhumation, crustal deformation and thermal structure of the Nepal Himalaya derived from the inversion of thermochronological and thermobarometric data and modeling of the topography, *J. Geophys. Res.*, *115*, B06407, doi:10.1029/2008JB006126.
- Herman, F., E. J. Rhodes, J. Braun, and L. Heiniger (2010b), Uniform erosion rates and relief amplitude during glacial cycles in the Southern Alps of New Zealand, as revealed from OSL-thermochronology, *Earth Planet. Sci. Lett.*, *297*, 183–189, doi:10.1016/j.epsl.2010.06.019.
- Hinderer, M. (2001), Late Quaternary denudation of the Alps, valley and lake fillings and modern river loads, *Geodin. Acta*, *14*, 231–263, doi:10.1016/S0985-3111(01)01070-1.
- Hurford, A. J. (1986), Cooling and uplift patterns in the Lepontine Alps, South Central Switzerland and an age of vertical movement on the Insubric fault line, *Contrib. Mineral. Petrol.*, *92*, 413–427, doi:10.1007/BF00374424.
- Hurford, A. J. (1991), Uplift and cooling pathways derived from fission track analysis and mica dating: A review, *Geol. Rundsch.*, *80*, 349–368, doi:10.1007/BF01829371.
- Jeannin, P.-Y. (1991), Mise en évidence d'importantes glaciations anciennes par l'étude des remplissages karstiques du Réseau des Siebenhengste (chaîne bordière helvétique), *Eclogae Geol. Helv.*, *84*, 207–221.
- Kahle, H. G., et al. (1997), Recent crustal movements, geoid and density distribution: Contribution from integrated satellite and terrestrial measurements, in *Deep Structure of the Swiss Alps: Results of NRP 20*, edited by O. A. Pfiffner et al., pp. 251–259, Birkhäuser, Basel, Switzerland.
- Kelly, M. A., J.-F. Buoncristiani, and C. Schluchter (2004), A reconstruction of the last glacial maximum (LGM) ice-surface geometry in the western Swiss Alps and contiguous Alpine regions in Italy and France, *Eclogae Geol. Helv.*, *97*, 57–75, doi:10.1007/s00015-004-1109-6.
- Ketcham, R. A. (2005), Forward and inverse modeling of low-temperature thermochronometry data, *Rev. Mineral. Geochem.*, *58*, 275–314, doi:10.2138/rmg.2005.58.11.
- Korup, O., and F. Schlunegger (2007), Bedrock landsliding, river incision, and transience of geomorphic hillslope-channel coupling: Evidence from inner gorges in the Swiss Alps, *J. Geophys. Res.*, *112*, F03027, doi:10.1029/2006JF000710.
- Kuhlemann, J., W. Frisch, B. Székely, I. Dunkl, and M. Kázmér (2002), Post-collisional sediment budget history of the Alps: Tectonic versus climatic control, *Int. J. Earth Sci.*, *91*, 818–837, doi:10.1007/s00531-002-0266-y.
- Kühni, A., and O. A. Pfiffner (2001a), The relief of the Swiss Alps and adjacent areas and its relation to lithology and structure: Topographic analysis from a 250-m DEM, *Geomorphology*, *41*, 285–307, doi:10.1016/S0169-555X(01)00060-5.
- Kühni, A., and O. A. Pfiffner (2001b), Drainage patterns and tectonic forcing: A model study for the Swiss Alps, *Basin Res.*, *13*, 169–197, doi:10.1046/j.1365-2117.2001.00146.x.
- Leloup, P. H., N. Arnaud, E. R. Sobel, and R. Lacassin (2005), Alpine thermal and structural evolution of the highest external crystalline massif: The Mont Blanc, *Tectonics*, *24*, TC4002, doi:10.1029/2004TC001676.
- Lisiecki, L. E. (2010), Links between eccentricity forcing and the 100,000-year glacial cycle, *Nat. Geosci.*, *3*, 349–352, doi:10.1038/ngeo828.
- Lisiecki, L. E., and M. E. Raymo (2005), A Pliocene-Pleistocene stack of 57 globally distributed benthic  $\delta^{18}\text{O}$  records, *Paleoceanography*, *20*, PA1003, doi:10.1029/2004PA001071.
- Mancktelow, N. (1985), The Simplon Line: A major displacement zone in the Western Lepontine Alps, *Eclogae Geol. Helv.*, *78*, 73–96.
- Mancktelow, N. S. (1992), Neogene lateral extension during convergence in the central Alps: Evidence from interrelated faulting and backfolding around the Simplon Pass (Switzerland), *Tectonophysics*, *215*, 295–317, doi:10.1016/0040-1951(92)90358-D.
- Mancktelow, N. S., and B. Grasemann (1997), Time-dependent effects of heat advection and topography on cooling histories during erosion, *Tectonophysics*, *270*, 167–195, doi:10.1016/S0040-1951(96)00279-X.
- Meesters, A. G. C. A., and T. J. Dunai (2002), Solving the production-diffusion equation for finite diffusion domains of various shapes: Part I. Implications for low-temperature (U–Th)/He thermochronology, *Chem. Geol.*, *186*, 333–344, doi:10.1016/S0009-2541(01)00422-3.
- Michalski, I., and M. Soom (1990), The Alpine thermo-tectonic evolution of the Aar and Gotthard massifs, Central Switzerland: Fission-Track ages on zircons and apatites and K–Ar mica ages, *Schweiz. Mineral. Petrogr. Mitt.*, *70*, 373–387.
- Molnar, P. (2004), Late Cenozoic increase in accumulation rates of terrestrial sediment: How might climate change have affected erosion rates?, *Annu. Rev. Earth Planet. Sci.*, *32*, 67–89, doi:10.1146/annurev.earth.32.091003.143456.
- Molnar, P., and P. England (1990), Late Cenozoic uplift of mountain ranges and global climate change: Chicken or egg?, *Nature*, *346*, 29–34, doi:10.1038/346029a0.
- Mudelsee, M., and M. E. Raymo (2005), Slow dynamics of the Northern Hemisphere glaciation, *Paleoceanography*, *20*, PA4022, doi:10.1029/2005PA001153.
- Muttoni, G., C. Carcano, E. Garzanti, M. Ghielmi, A. Piccin, R. Pini, S. Rogledi, and D. Sciuannach (2003), Onset of major Pleistocene glaciations in the Alps, *Geology*, *31*, 989–992, doi:10.1130/G19445.1.
- Nocquet, J.-M., and E. Calais (2004), Geodetic measurements of crustal deformation in the western Mediterranean and Europe, *Pure Appl. Geophys.*, *161*, 661–681, doi:10.1007/s00024-003-2468-z.
- Norton, K. P., L. M. Abbühl, and F. Schlunegger (2010), Glacial conditioning as an erosional driving force in the central Alps, *Geology*, *38*, 655–658, doi:10.1130/G31102.1.
- Persaud, M., and O. A. Pfiffner (2004), Active deformation in the eastern Swiss Alps: Post-glacial faults, seismicity and surface uplift, *Tectonophysics*, *385*, 59–84, doi:10.1016/j.tecto.2004.04.020.
- Pfiffner, O. A., P. Heitzmann, P. Lehner, W. Frei, A. Pugin, and M. Felber (1997), Incision and backfilling of Alpine valleys: Pliocene, Pleistocene and Holocene processes, in *Deep Structure of the Swiss Alps: Results of NRP 20*, edited by O. A. Pfiffner, pp. 265–288, Birkhäuser, Basel, Switzerland.
- Pfiffner, O. A., F. Schlunegger, and S. J. H. Buitter (2002), The Swiss Alps and their peripheral foreland basin: Stratigraphic response to deep crustal processes, *Tectonics*, *21*(2), 1009, doi:10.1029/2000TC900039.
- Pignalosa, A., M. Zattin, M. Massironi, and W. Cavazza (2011), Thermochronological evidence for a late Pliocene climate-induced erosion rate increase in the Alps, *Int. J. Earth Sci.*, *100*, 847–859, doi:10.1007/s00531-010-0510-9.
- Rahn, M. K. (1994), Incipient metamorphism of the Glarus Alps: Petrology of the Taveyenne Greywacke and fission track dating, Ph.D. thesis, 209 pp., Univ. of Basel, Basel, Switzerland.
- Raymo, M. W., and W. F. Ruddiman (1992), Tectonic forcing of late Cenozoic climate, *Nature*, *359*, 117–122, doi:10.1038/359117a0.

- Reinecker, J., M. Danišik, C. Schmid, C. Glotzbach, M. Rahn, W. Frisch, and C. Spiegel (2008), Tectonic control on the late stage exhumation of the Aar Massif (Switzerland): Constraints from apatite fission track and (U-Th)/He data, *Tectonics*, 27, TC6009, doi:10.1029/2007TC002247.
- Rosselli, A., and R. Olivier (2003), Modélisation gravimétrique 2.5D et cartes isohypses au 1:100'000 du substratum rocheux de la Vallée du Rhône entre Villeneuve et Brig (Suisse), *Eclogae Geol. Helv.*, 96, 399–423.
- Rybach, L., D. Werner, S. Mueller, and G. Berset (1977), Heat flow, heat production and crustal dynamics in the central Alps Switzerland, *Tectonophysics*, 41, 113–126, doi:10.1016/0040-1951(77)90183-4.
- Sambridge, M. (1999a), Geophysical inversion with a neighbourhood algorithm—I. Searching a parameter space, *Geophys. J. Int.*, 138, 479–494, doi:10.1046/j.1365-246X.1999.00876.x.
- Sambridge, M. (1999b), Geophysical inversion with a neighbourhood algorithm—II. Appraising the ensemble, *Geophys. J. Int.*, 138, 727–746, doi:10.1046/j.1365-246X.1999.00900.x.
- Schildgen, T. F., G. Balco, and D. L. Shuster (2010), Canyon incision and knickpoint propagation recorded by apatite  $^4\text{He}/^3\text{He}$  thermochronometry, *Earth Planet. Sci. Lett.*, 293, 377–387, doi:10.1016/j.epsl.2010.03.009.
- Schlatter, A., D. Schneider, A. Geiger, and H.-G. Kahle (2005), Recent vertical movements from precise levelling in the vicinity of the city of Basel, Switzerland, *Int. J. Earth Sci.*, 94, 507–514, doi:10.1007/s00531-004-0449-9.
- Schlüchter, C. (1986), The Quaternary glaciations of Switzerland, with special reference to the northern alpine foreland, *Quat. Sci. Rev.*, 5, 413–419.
- Schlunegger, F., and M. Hinderer (2001), Crustal uplift in the Alps: Why the drainage pattern matters, *Terra Nova*, 13, 425–432, doi:10.1046/j.1365-3121.2001.00374.x.
- Schlunegger, F., and M. Hinderer (2003), Pleistocene/Holocene climate change, reestablishment of fluvial drainage network and increase in relief in the Swiss Alps, *Terra Nova*, 15, 88–95, doi:10.1046/j.1365-3121.2003.00469.x.
- Schlunegger, F., and J. Mosar (2011), The last erosional stage of the Molasse Basin and the Alps, *Int. J. Earth Sci.*, 100, 1147–1162, doi:10.1007/s00531-010-0607-1.
- Schmid, S. M., and E. Kissling (2000), The arc of the Western Alps in the light of geophysical data on deep crustal structure, *Tectonics*, 19, 62–85, doi:10.1029/1999TC900057.
- Schmid, S. M., O. A. Pfiffner, N. Froitzheim, G. Schönborn, and E. Kissling (1996), Geophysical geological transect and tectonic evolution of the Swiss-Italian Alps, *Tectonics*, 15, 1036–1064, doi:10.1029/96TC00433.
- Schmid, S. M., B. Fügenschuh, E. Kissling, and R. Schuster (2004), Tectonic map and overall architecture of the Alpine orogeny, *Eclogae Geol. Helv.*, 97, 93–117, doi:10.1007/s00015-004-1113-x.
- Schwarz, G. (1978), Estimating the dimension of a model, *Ann. Stat.*, 6, 461–464, doi:10.1214/aos/1176344136.
- Seward, D., and N. S. Mancktelow (1994), Neogene kinematics of the central and Western Alps: Evidence from fission-track dating, *Geology*, 22, 803–806, doi:10.1130/0091-7613(1994)022<0803:NKOTCA>2.3.CO;2.
- Shuster, D. L., and K. A. Farley (2004),  $^4\text{He}/^3\text{He}$  thermochronometry, *Earth Planet. Sci. Lett.*, 217, 1–17, doi:10.1016/S0012-821X(03)00595-8.
- Shuster, D. L., and K. A. Farley (2005),  $^4\text{He}/^3\text{He}$  thermochronometry: Theory, practice, and potential complications, in *Low-Temperature Thermochronology: Techniques, Interpretations, and Applications*, *Rev. Mineral. Geochem.*, vol. 58, edited by P. W. Reiners and T. A. Ehlers, pp. 181–203, Mineral. Soc. of Am., Washington, D. C.
- Shuster, D. L., and K. A. Farley (2009), The influence of artificial radiation damage and thermal annealing on helium diffusion kinetics in apatite, *Geochim. Cosmochim. Acta*, 73, 183–196, doi:10.1016/j.gca.2008.10.013.
- Shuster, D. L., K. A. Farley, J. M. Sistierson, and D. S. Burnett (2004), Quantifying the diffusion kinetics and spatial distributions of radiogenic  $^4\text{He}$  in minerals containing proton-induced  $^3\text{He}$ , *Earth Planet. Sci. Lett.*, 217, 19–32, doi:10.1016/S0012-821X(03)00594-6.
- Shuster, D. L., T. A. Ehlers, M. E. Rusmore, and K. A. Farley (2005), Rapid glacial erosion at 1.8 Ma revealed by  $^4\text{He}/^3\text{He}$  thermochronometry, *Science*, 310, 1668–1670, doi:10.1126/science.1118519.
- Shuster, D. L., R. M. Flowers, and K. A. Farley (2006), The influence of natural radiation damage on helium diffusion kinetics in apatite, *Earth Planet. Sci. Lett.*, 249, 148–161, doi:10.1016/j.epsl.2006.07.028.
- Shuster, D. L., K. M. Cuffey, J. W. Sanders, and G. Balco (2011), Thermochronometry reveals headward propagation of erosion in an alpine landscape, *Science*, 332, 84–88, doi:10.1126/science.1198401.
- Small, E., and R. S. Anderson (1998), Pleistocene relief production in Laramide mountain ranges, western United States, *Geology*, 26, 123–126, doi:10.1130/0091-7613(1998)026<0123:PRPILM>2.3.CO;2.
- Sonney, R., and F.-D. Vuattaz (2009), Numerical modelling of Alpine deep flow systems: A management and prediction tool for an exploited geothermal reservoir (Lavey-les-Bains, Switzerland), *Hydrogeol. J.*, 17, 601–616, doi:10.1007/s10040-008-0394-y.
- Soom, M. A. (1990), Abkühlungs- und Hebungsgeschichte der Externmassive und der penninischen Decken beidseits der Simplon-Rhone-Linie seit dem Oligozän: Spaltspurdatering an Apatit/Zirkon und K-Ar-Datierungen an Biotit/Muskovit (westliche Zentralalpen), Ph.D. thesis, 64 pp., Univ. of Bern, Bern, Switzerland.
- Stampfli, G. M., J. Mosar, D. Marquer, R. Marchant, T. Baudin, and G. Borel (1998), Subduction and obduction processes in the Swiss Alps, *Tectonophysics*, 296, 159–204, doi:10.1016/S0040-1951(98)00142-5.
- Stephenson, J., K. Gallagher, and C. C. Holmes (2006), A Bayesian approach to calibrating apatite fission track annealing models for laboratory and geological timescales, *Geochim. Cosmochim. Acta*, 70, 5183–5200, doi:10.1016/j.gca.2006.07.027.
- Stewart, J., and A. B. Watts (1997), Gravity anomalies and spatial variation of flexural rigidity at mountain ranges, *J. Geophys. Res.*, 102, 5327–5352, doi:10.1029/96JB03664.
- Sue, C., B. Delacou, J.-D. Champagnac, C. Allanic, P. Tricart, and M. Burkhard (2007), Extensional neotectonics around the bend of the Western/central Alps: An overview, *Int. J. Earth Sci.*, 96, 1101–1129, doi:10.1007/s00531-007-0181-3.
- Tesauro, M., M. K. Kaban, and S. P. A. L. Cloetingh (2008), EuCRUST-07: A new reference model for the European crust, *Geophys. Res. Lett.*, 35, L05313, doi:10.1029/2007GL032244.
- Valla, P. G., F. Herman, P. A. van der Beek, and J. Braun (2010a), Inversion of thermochronological age-elevation profiles to extract independent estimates of denudation and relief history—I: Theory and conceptual model, *Earth Planet. Sci. Lett.*, 295, 511–522, doi:10.1016/j.epsl.2010.04.033.
- Valla, P. G., P. A. van der Beek, and D. Lague (2010b), Fluvial incision into bedrock: Insights from morphometric analysis and numerical modeling of gorges incising glacial hanging valleys (Western Alps, France), *J. Geophys. Res.*, 115, F02010, doi:10.1029/2008JF001079.
- Valla, P. G., D. L. Shuster, and P. A. van der Beek (2011a), Major increase in relief of the European Alps during mid-Pleistocene glaciations recorded by apatite  $^4\text{He}/^3\text{He}$  thermochronometry, *Nat. Geosci.*, 4, 688–692, doi:10.1038/ngeo1242.
- Valla, P. G., P. A. van der Beek, and J. Braun (2011b), Rethinking low-temperature thermochronology data sampling and modelling strategies for quantification of denudation and relief histories, *Earth Planet. Sci. Lett.*, 307, 309–322, doi:10.1016/j.epsl.2011.05.003.
- van der Beek, P. A., and P. Bourbon (2008), A quantification of the glacial imprint on relief development in the French Western Alps, *Geomorphology*, 97, 52–72, doi:10.1016/j.geomorph.2007.02.038.
- van der Beek, P. A., P. G. Valla, F. Herman, J. Braun, C. Persano, K. J. Dobson, and E. Labrin (2010), Inversion of thermochronological age-elevation profiles to extract independent estimates of denudation and relief history—II: Application to the French Western Alps, *Earth Planet. Sci. Lett.*, 296, 9–22, doi:10.1016/j.epsl.2010.04.032.
- Vernon, A. J., P. A. van der Beek, H. D. Sinclair, and M. K. Rahn (2008), Increase in late Neogene denudation of the European Alps confirmed by analysis of a fission track thermochronology database, *Earth Planet. Sci. Lett.*, 270, 316–329, doi:10.1016/j.epsl.2008.03.053.
- Vernon, A. J., P. A. van der Beek, H. D. Sinclair, C. Persano, J. Foecken, and F. M. Stuart (2009), Variable late Neogene exhumation of the central European Alps: Low-temperature thermochronology from the Aar Massif, Switzerland, and the Lepontine Dome, Italy, *Tectonics*, 28, TC5004, doi:10.1029/2008TC002387.
- Viganò, A., and S. Martin (2007), Thermorheological model for the European central Alps: Brittle-ductile transition and lithospheric strength, *Terra Nova*, 19, 309–316, doi:10.1111/j.1365-3121.2007.00751.x.
- von Raumer, J. F., and F. Neubauer (1993), *Pre-Mesozoic Geology in the Alps*, 677 pp., Springer, New York.
- Vuattaz, F.-D., J.-D. Rouiller, J.-D. Dubois, G. Bianchetti, and O. Besson (1993), Programme Géothermoval: Résultats d'une prospection des ressources géothermiques du Valais, Suisse, *Bull. Cent. Hydrogeol. Univ. Neuchâtel*, 12, 1–37.
- Wagner, G. A., G. M. Reimer, and E. Jäger (1977), Cooling ages derived by apatite fission track, mica Rb-Sr and K-Ar dating: The uplift and cooling history of the central Alps, *Mem. Sci. Geol.*, 30, 1–27.
- Whipp, D. M., and T. A. Ehlers (2007), Influence of groundwater flow on the thermochronometer-derived exhumation rates in the central Nepalese Himalaya, *Geology*, 35, 851–854, doi:10.1130/G23788A.1.
- Whipple, K. X. (2009), The influence of climate on the tectonic evolution of mountain belts, *Nat. Geosci.*, 2, 97–104, doi:10.1038/ngeo413.
- Whipple, K. X., and B. J. Meade (2006), Orogen response to changes in climatic and tectonic forcing, *Earth Planet. Sci. Lett.*, 243, 218–228, doi:10.1016/j.epsl.2005.12.022.

- Willett, S. D. (1999), Orogeny and orography: The effects of erosion on the structure of mountain belts, *J. Geophys. Res.*, *104*, 28,957–28,981, doi:10.1029/1999JB900248.
- Willett, S. D., and M. T. Brandon (2002), On steady states in mountain belts, *Geology*, *30*, 175–178, doi:10.1130/0091-7613(2002)030<0175:OSSIMB>2.0.CO;2.
- Willett, S. D., F. Schlunegger, and V. Picotti (2006), Messinian climate change and erosional destruction of the central European Alps, *Geology*, *34*, 613–616, doi:10.1130/G22280.1.
- Wittmann, H., F. von Blanckenburg, T. Kruesmann, K. P. Norton, and P. W. Kubik (2007), Relation between rock uplift and denudation from cosmogenic nuclides in river sediment in the central Alps of Switzerland, *J. Geophys. Res.*, *112*, F04010, doi:10.1029/2006JF000729.
- Wolf, R. A., K. A. Farley, and D. M. Kass (1998), Modeling of the temperature sensitivity of the apatite (U-Th)/He thermochronometer, *Chem. Geol.*, *148*, 105–114, doi:10.1016/S0009-2541(98)00024-2.
- Zhang, P., P. Molnar, and W. R. Downs (2001), Increased sedimentation rates and grain sizes 2–4 Myr ago due to the influence of climate change on erosion rates, *Nature*, *410*, 891–897, doi:10.1038/35073504.
- Zuccoli, L. (2000), Geology of the high plains of Castelseprio and Tradate (northern Italy), *Ital. J. Quat. Sci.*, *13*, 57–80.
- 
- J. Braun and P. A. van der Beek, Institut des Sciences de la Terre, Université Joseph Fourier, CNRS, BP 53, F-38041 Grenoble, France.
- C. Gautheron, Interactions et Dynamique des Environnements de Surface, Université Paris Sud, CNRS, F-91405 Orsay, France.
- F. Herman and P. G. Valla, Geologisches Institut, ETH Zurich, Sonneggstr. 5, Zürich CH-8092, Switzerland. (pierre.valla@erdw.ethz.ch)
- D. L. Shuster, Berkeley Geochronology Center, 2455 Ridge Rd., Berkeley, CA 94709, USA.
- L. Tassan-Got, Institut de Physique Nucléaire, Université Paris Sud, CNRS/IN2P3, F-91405 Orsay, France.